

# The birth mass function of neutron stars

Zhi-Qiang You<sup>1,2,3,4</sup>, Xingjiang Zhu<sup>1,2,5\*</sup>, Xiaojin Liu<sup>1,2,3</sup>, Bernhard Müller<sup>6,7</sup>, Alexander Heger<sup>6,7</sup>, Simon Stevenson<sup>7,8</sup>, Eric Thrane<sup>6,7</sup>, Zu-Cheng Chen<sup>1,2,3,9,10</sup>, Ling Sun<sup>7,11</sup>, Paul Lasky<sup>6,7</sup>, Duncan K. Galloway<sup>6,7,12</sup>, George Hobbs<sup>13</sup>, Richard N. Manchester<sup>13</sup>, He Gao<sup>3,5</sup>, Zong-Hong Zhu<sup>3,14†</sup>

<sup>1</sup>*Department of Physics, Faculty of Arts and Sciences, Beijing Normal University, Zhuhai 519087, China*

<sup>2</sup>*Advanced Institute of Natural Sciences, Beijing Normal University, Zhuhai 519087, China*

<sup>3</sup>*School of Physics and Astronomy, Beijing Normal University, Beijing 100875, China*

<sup>4</sup>*Henan Academy of Sciences, Zhengzhou 450046, Henan, China*

<sup>5</sup>*Institute for Frontier in Astronomy and Astrophysics, Beijing Normal University, Beijing 102206, China*

<sup>6</sup>*School of Physics and Astronomy, Monash University, Clayton, VIC 3800, Australia*

<sup>7</sup>*OzGrav: The ARC Centre of Excellence for Gravitational Wave Discovery, Hawthorn, VIC 3122, Australia*

<sup>8</sup>*Centre for Astrophysics and Supercomputing, Swinburne University of Technology, P.O. Box 218, Hawthorn, VIC 3122, Australia*

<sup>9</sup>*Department of Physics and Synergetic Innovation Center for Quantum Effects and Applications, Hunan Normal University, Changsha, China.*

---

\*E-mail: zhuxj@bnu.edu.cn

†E-mail: zhuzh@bnu.edu.cn

<sup>10</sup>*Institute of Interdisciplinary Studies, Hunan Normal University, Changsha, China*

<sup>11</sup>*Centre for Gravitational Astrophysics, College of Science, The Australian National University, Canberra, Australian Capital Territory, Australia.*

<sup>12</sup>*Institute for Globally Distributed Open Research and Education (IGDORE), Gothenburg, Sweden.*

<sup>13</sup>*Australia Telescope National Facility, CSIRO Space and Astronomy, Epping, New South Wales, Australia.*

<sup>14</sup>*School of Physics and Technology, Wuhan University, Wuhan, Hubei 430072, China*

**The birth mass function of neutron stars encodes rich information about supernova explosions, double-star evolution and properties of matter under extreme conditions. To date, it has remained poorly constrained by observations, however. Applying probabilistic corrections to account for mass accreted by recycled pulsars in binary systems to mass measurements of 90 neutron stars, we find that the birth masses of neutron stars can be described by a unimodal distribution that smoothly turns on at  $1.1 M_{\odot}$ , peaks at  $\sim 1.27 M_{\odot}$ , before declining as a steep power law. Such a “turn-on” power-law distribution is strongly favoured against the widely adopted empirical double-Gaussian model at the  $3\sigma$  level. The power-law shape may be inherited from the initial mass function of massive stars<sup>1,2</sup>, but the relative dearth of massive neutron stars implies that single stars with initial masses greater than  $\sim 18 M_{\odot}$  do not form neutron stars, in agreement with the absence of massive red supergiant progenitors of supernovae<sup>3,4</sup>.**

The observational determination of mass function of neutron stars is a long-standing problem in astrophysics. Early attempts were able to derive only loose constraints on the range of possible neutron star masses from a small number of measurements<sup>5,6</sup>. For a long time, all observed neutron-stars masses were in a narrow range, consistent with a Gaussian distribution with a mean of  $1.35 M_{\odot}$  and a width of  $0.04 M_{\odot}$  (ref.<sup>7</sup>). Owing partly to the precise mass measurements of the Hulse-Taylor binary pulsar<sup>8,9</sup>, a canonical mass of  $1.4 M_{\odot}$  has routinely been adopted in most current studies of neutron stars and in textbooks.

As the number of neutron-star mass measurements steadily increased, especially with the

discoveries of massive neutron stars around  $2 M_{\odot}$  (refs. <sup>10,11</sup>), it became apparent that the single-Gaussian model could no longer fit all available data. Various groups have started to employ a two-Gaussian (2G) model to explain the observations, with the secondary mass peak shifting to higher values as more massive neutron stars have been measured<sup>12–15</sup>. The most widely adopted model consists of a narrow peak at  $1.4 M_{\odot}$  and a broad peak at  $1.8 M_{\odot}$  (ref. <sup>16</sup>), and the two peaks are attributed to different formation channels and evolutionary histories of the neutron stars<sup>17</sup>.

From a theoretical perspective, the neutron-star mass function is a powerful probe into supernova physics, compact binary evolution and the neutron-star equation of state. It was once proposed that the two low-mass peaks (at  $1.25 M_{\odot}$  and  $1.35 M_{\odot}$ ) claimed in the mass distribution are the product of distinct supernova progenitor channels, electron-capture supernovae and low-mass iron-core-collapse supernovae<sup>18,19</sup>. An additional high-mass peak centred around  $1.8 M_{\odot}$  in the mass distribution was thought to arise due to the transition from convective central carbon burning to radiative central carbon burning<sup>18,20</sup>. Recent detailed studies, however, have revealed a complicated landscape of interacting shells with discontinuous changes in the core and remnant masses when the number of shells changes, or shells merge, as a function of initial or helium core mass<sup>21,23</sup>.

Efforts to link the observed mass distribution to neutron star formation channels are complicated because the fact that neutron stars in binary systems often go through a recycling

process and gain some mass through accretion<sup>24–27</sup>. Such a recycling process is the standard formation pathway for millisecond pulsars, which have by far dominated the population of neutron stars with precise mass measurements. Although the recycling process may increase the neutron-star mass by up to  $\sim 0.3 M_{\odot}$  (refs.<sup>24,27,28</sup>), it has been argued that the high-mass peak around  $1.8 M_{\odot}$  in the observed mass spectrum is probably not caused by mass accretion but, instead, a hint of neutron stars being born massive<sup>15</sup>. Current supernova simulations, however, have difficulties in producing enough neutron stars around  $1.8 M_{\odot}$  as implied by the empirical 2G model<sup>29</sup>.

To determine the neutron-star mass distribution, we compiled a sample of 90 neutron stars for which well-determined mass estimates are available from observations of radio pulsars, gravitational waves and X-ray binaries. For most of the neutron stars in our sample, the observed spin properties allowed us to securely categorize them into two subclasses: recycled and non-recycled (slowly rotating) neutron stars. The first class is characterized by rapid spins (period  $P \lesssim 100$  ms), whereas the second class includes neutron stars with spin periods of the order of seconds or longer. When constraining the birth-mass function of neutron stars, the key difference between the two subclasses is that observed masses of recycled pulsars need to be corrected for mass accreted throughout the recycling process, whereas the measured masses of slow neutron stars should equal their birth masses, as no mass-gaining process occurred. See Section A, Extended Data Tables 1 and 2 for details.

Figure 1 shows the distributions of measured masses (black lines with grey-shaded areas) and estimated birth masses (blue lines) for 39 recycled pulsars. In each subplot, we also list the pulsar name, observed spin period and plausible initial spin period. The birth masses of recycled pulsars were estimated by subtracting accreted masses from their measured masses. We adopted an analytical approach for estimating the accreted mass. To the leading order, the total amount of accreted mass scales inversely with the final equilibrium spin period in the recycling process. Based on the simple accretion spin-up theory<sup>24,27,30</sup>, we derived the probability distribution of the accreted mass by accounting for uncertainties in the accretion rate, neutron star moment of inertia, magnetic inclination angle and accretion disk-magnetosphere interactions. See Section B and Extended Data Figs 1, 2 and 3.

We fitted a variety of models to the mass distribution of neutron stars. The Gaussian models are a 2G distribution with both a low- and high-mass cutoff ( $2G_{\min}^{\max}$ ), a 2G distribution with a low-mass cutoff ( $2G_{\min}$ ) and a 2G distribution with a high-mass cutoff ( $2G^{\max}$ ). In addition to the Gaussian-family models, we considered a turn-on power-law(TOP) distribution, which allows an exponential turn-on from the minimum mass<sup>31</sup>, as well as a skewed Student's  $t$ -distribution. Some of the models are illustrated in panel **b** of Figure 2. Bayesian model selection was performed to find the model that best describes the data. The Bayes factors, which quantify the statistical support for one model against another, between five top-performing models and the empirical two-Gaussian (2G) model are shown in panel **a** of Figure 2. The best-performing model was the turn-on power law (TOP), which is preferred against the 2G model with a Bayes

factor greater than 300. Assuming equal prior probabilities for both models, this result means an odds of 0.003, or equivalently  $\sim 3\sigma$  significance. Potential selection effects are discussed in Section G of Methods, and further details can be found in Extended Data Figure 10.

Figure 3 shows the reconstructed birth-mass function of neutron star for the turn-on power law model, as well as histograms for two different bin sizes. We found that the minimum mass was  $1.1_{-0.05}^{+0.04} M_{\odot}$ . The distribution peaked at  $1.27_{-0.04}^{+0.03} M_{\odot}$  and declined with a power-law index of  $6.5_{-1.2}^{+1.3}$ . We found marginal evidence for a maximum-mass cutoff, with a Bayes factor of 2. The maximum mass was loosely constrained to be  $2.36_{-0.17}^{+0.29} M_{\odot}$ . (All numbers quoted are median and  $1\sigma$  credible intervals.) The posterior distributions of model parameters are presented in Figure 4. We found no evidence for other peaks on top of the power-law function, although such a possibility cannot be ruled out either.

The final evolution of the lowest-mass stars that make iron-core-collapse supernovae is notably diverse and a challenge to model due to the complicated physics<sup>32</sup>. Hence, any constraints from observations on this mass regime are invaluable. Such low-mass iron-core-collapse supernovae are predicted to produce neutron stars with masses as low as or potentially below  $1.15 M_{\odot}$  (refs.<sup>18,32</sup>), consistent with our observed minimum. Electron-capture supernovae are unlikely to produce such low-mass neutron stars<sup>33</sup>. They, however, may make neutron stars with masses within the peak of the distribution. The data presently do not provide support for the two discrete low-mass peaks that are expected from theoretical calculations<sup>19</sup>. Instead, the distribu-

tion is probably a superposition of several overlapping discontinuous (as a function of initial mass) contributions<sup>21,23</sup>, overlaid with some scatter due to variations in the turbulent supernova explosions<sup>34</sup>. Particularly marked is the absence of the second peak predicted at  $1.35 M_{\odot}$ , which probably hints at the larger importance of lower-mass core-collapse and of stripped-core supernova progenitors<sup>35</sup>.

If we accept the core structures predicted by current stellar evolution models, the absence of prominent peaks and the measured power-law slope of the neutron-star mass distribution have important implications for supernova explosion physics. Specifically, the most parsimonious explanation of TOP is that neutron stars from more massive progenitors undergo substantial net accretion during the explosion and that explosions occur only for stars with main sequence masses of  $\lesssim 18 M_{\odot}$  in agreement with the observed absence of massive red supergiants as progenitors for core-collapse supernovae<sup>3,4</sup> or for stripped stars with similar core structures. We demonstrate this through the use of semi-analytic supernova models<sup>21</sup>, as described in Methods Section F.

Knowing the neutron-star mass function is also essential for understanding the population of binary neutron star mergers observed by their gravitational wave signal. A fraction of these mergers result in stable very high-mass neutron stars. It also allows us to obtain a more accurate prediction of the frequency band for post-merger gravitational-wave signals, which can substantially benefit the design and optimization of future-generation gravitational-wave obser-

vatories that aim to probe post-merger physics<sup>37-39</sup>. The remnant compact object formed in a binary neutron star merger is in an extreme, high-density, high-energy state and encodes unique information about nuclear matter that the progenitor stars and the inspiral phase do not provide. Observations of the post-merger gravitational waves may provide unprecedented opportunities for exploring hot equations of state at supranuclear densities and identifying phase transitions in extreme nuclear matter<sup>40-42</sup>. The post-merger emissions are at frequencies mainly determined by the progenitor neutron-star masses and the yet unknown nuclear equation of state, spanning a wide range roughly from 1 to 4 kHz (refs.<sup>43,44</sup>).

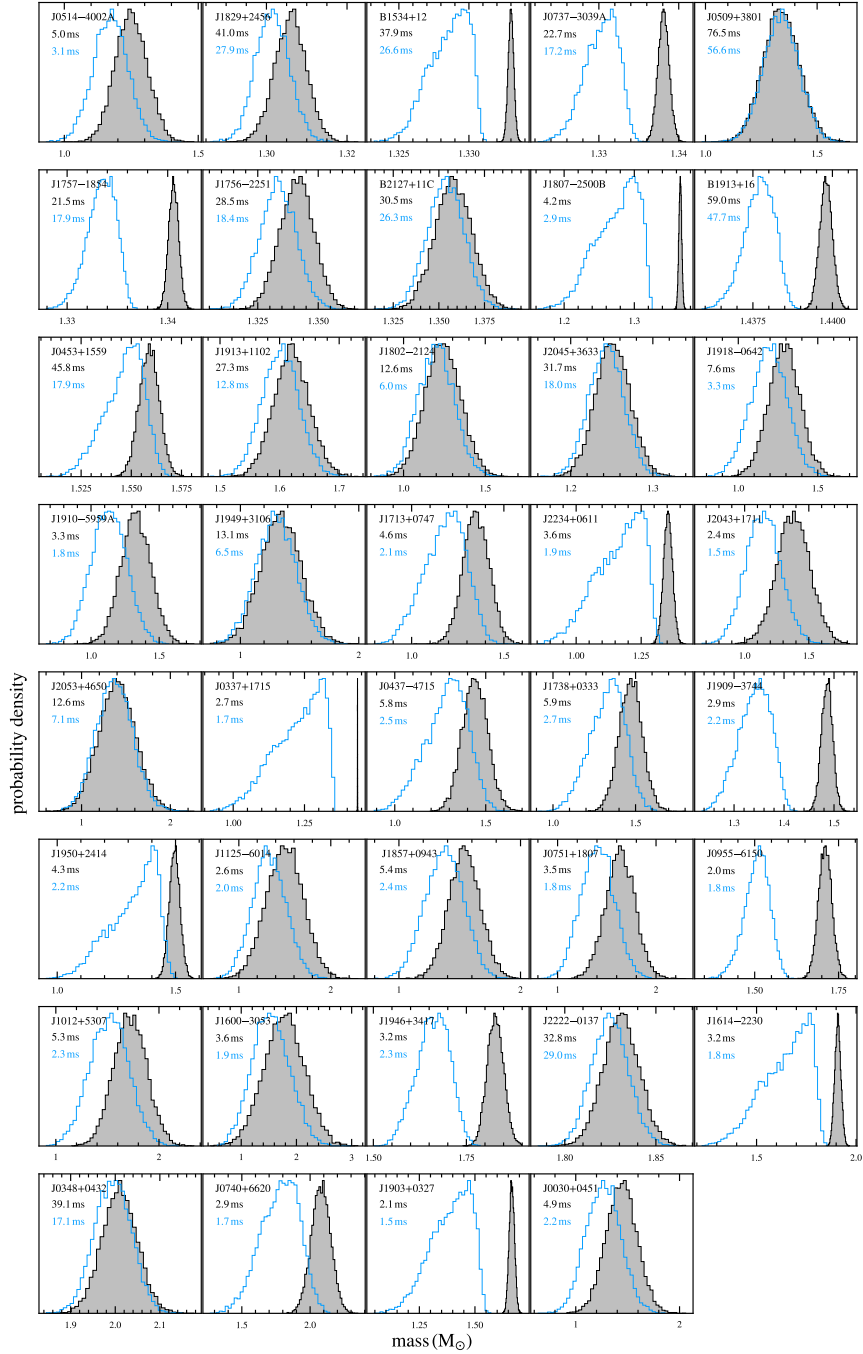


**Figure 1 Individual mass distributions of 39 recycled pulsars.** Black lines with grey shaded area are measured masses, whereas blue lines are estimated birth masses after subtracting accreted masses based on the analytical prescription. Observed and plausible initial spin periods, along with pulsar names are given in each subplot. For readability, we scale different posteriors to the same  $y$  coordinate height.



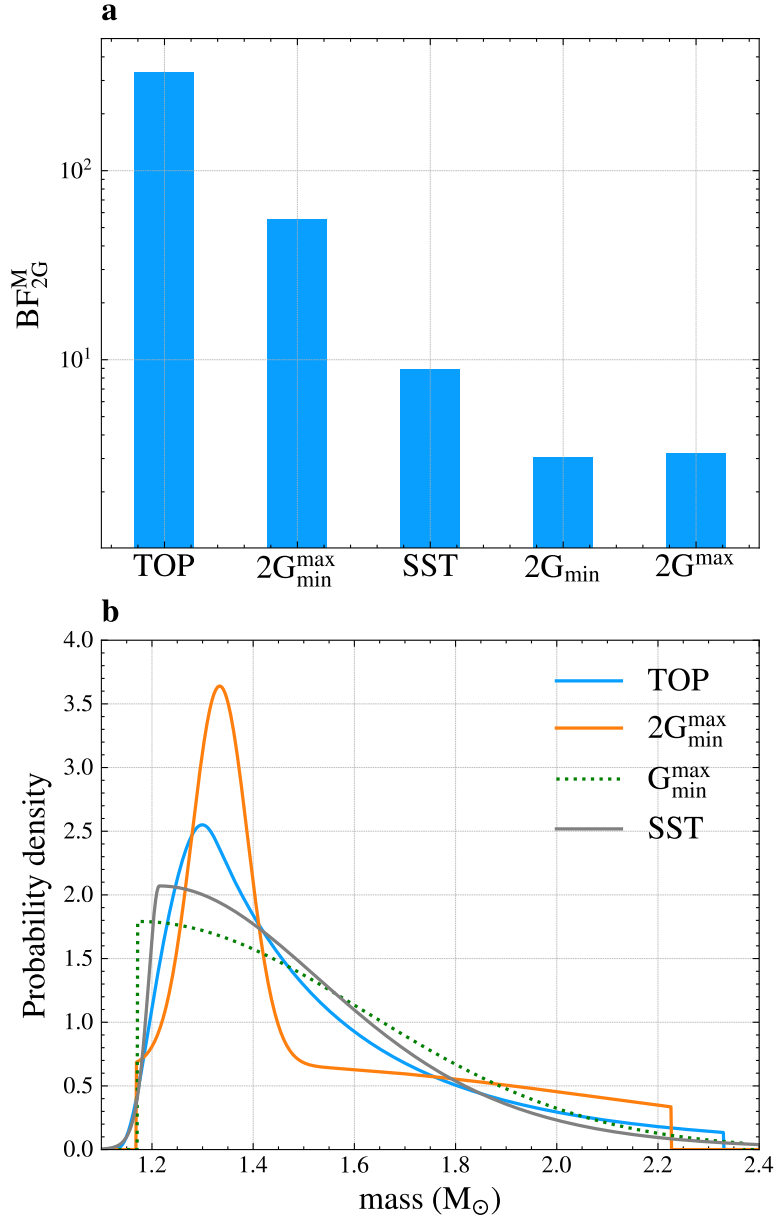


**Figure 2 Example mass models and their Bayes factors.** **a**, Bayes factor between various models (M) and the 2G model for the birth mass function of neutron stars. **b**, Mass models. In addition to the models listed in **a**, we also show a single-Gaussian distribution with both a low- and high-mass cutoff ( $G_{\min}^{\max}$ ). Model parameters were set to their maximum-likelihood values inferred from data. SST, skewed Student's  $t$ -distribution.

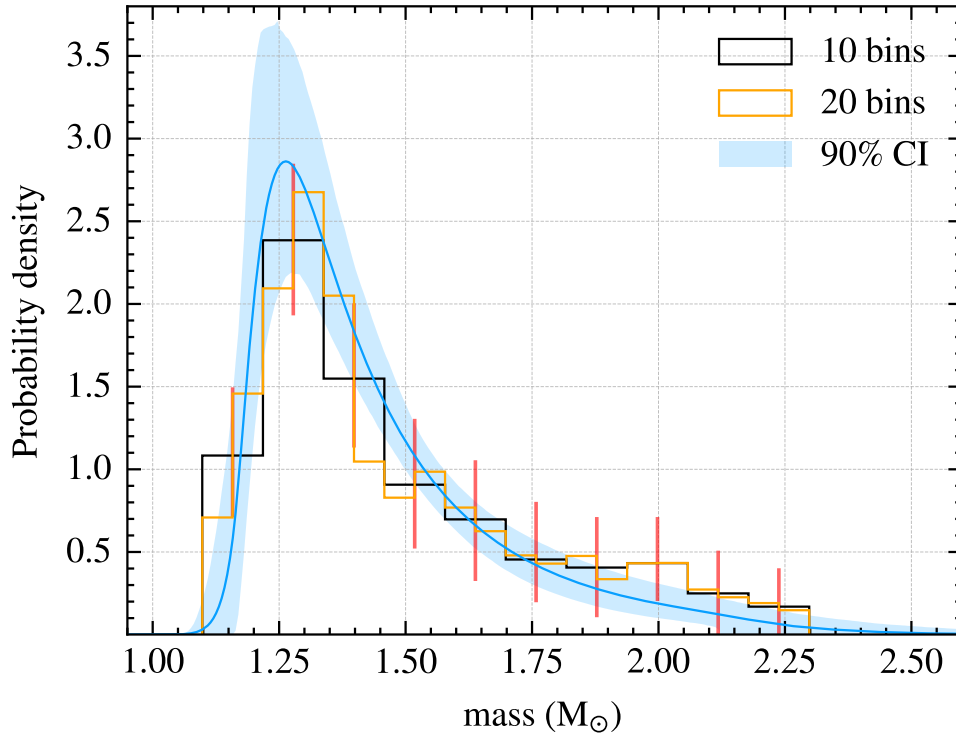


**Figure 3** Reconstructed birth-mass function of neutron stars based on the preferred TOP model. The solid blue line shows the population predictive distribution, whereas the shaded blue band indicates the 90% credible interval. Also plotted are a ten-bin histogram (mean value) with 90% credibility error bars and a 20-bin histogram (mean value) for the data, showing the robustness of our model in fitting the underlying distribution. CI, confidence interval.

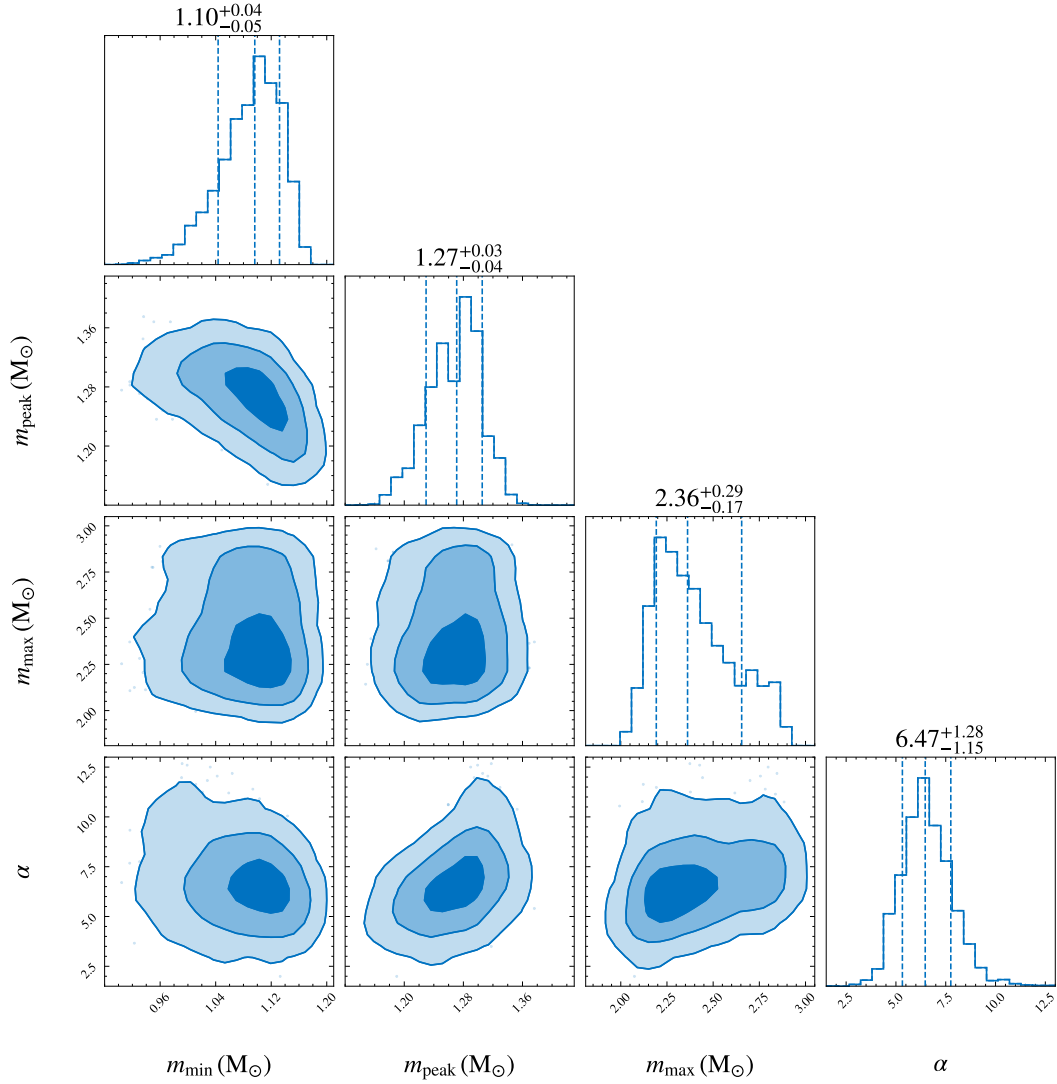


**Figure 4** Posterior distribution of the TOP model parameters. Shown are the minimum neutron-star mass  $m_{\min}$ , the peak of the mass function  $m_{\text{peak}}$ , the maximum mass  $m_{\text{max}}$  and the power-law index  $\alpha$ .

**Data Availability** All the neutron-star mass measurements used in this study are listed in Extended Data Tables 1 and 2 with the original references. These mass measurements, accreted-mass corrections for recycled pulsars, posterior samples from Bayesian inference and the data behind Extended Data Tables 1 and 2 and Figures 1–4 and Extended Data Figures 1–4 are available via Zenodo at <https://doi.org/10.5281/zenodo.14375273>. Source data are provided with this paper.

**Code Availability** The following open-source software packages were used in this paper: [GalDynPsr](#), [gwpopulation](#), [BILBY](#) and [dynesty](#). The Python scripts used for data analysis and figure generation are publicly available via GitHub at <https://github.com/GW-BNUZ/NSbirthMass>.

**Acknowledgements** We thank Z. Li, X. Chen and Z. Han for providing data from their numerical simulations, which are plotted in Extended Data Figure 2. We also thank I. Mandel and M. Bailes for useful discussions. This work was supported by the National Natural Science Foundation of China (Grant Nos. 12203004 to X.Z., 12021003 and 12433001 to Z.-H.Z., 12305059 to Z.-Q.Y. and 12405056 to Z.-C.C.). X.Z. and H.G. are supported by the Fundamental Research Funds for the Central Universities. This work was supported in part by the Australian Research Council (ARC) Centre of Excellence for Gravitational Wave Discovery (Project Nos. CE170100004 and CE230100016). S.S. is a recipient of an ARC Discovery Early Career Research Award (DE220100241). This work was supported by ARC Discovery Grants DP240101786 (to B.M. and A.H.) and DP240103174 (to A.H.).

**Author Contributions** All authors contributed to the work presented in this paper.

**Competing Interests** The authors declare no competing interests.

1. Kroupa, P. On the variation of the initial mass function. *Mon. Not. R. Astron. Soc.* 231–246 (2001). [astro-ph/0009005](#).
2. Schneider, F. R. N. *et al.* An excess of massive stars in the local 30 Doradus starburst. *Science* **359**, 69–71 (2018). [1801.03107](#).
3. Smartt, S. J., Eldridge, J. J., Crockett, R. M. & Maund, J. R. The death of massive stars - I. Observational constraints on the progenitors of Type II-P supernovae. *Mon. Not. R. Astron. Soc.* **395**, 1409–1437 (2009). [0809.0403](#).
4. Davies, Ben & Beasar, Emma R. The initial masses of the red supergiant progenitors to Type II supernovae. *Mon. Not. R. Astron. Soc.* **474**, 2116–2128 (2018). [1709.06116](#).
5. Joss, P. C. & Rappaport, S. A. Observational constraints on the masses of neutron stars. *Nat.* **264**, 219–222 (1976).
6. Finn, L. S. Observational constraints on the neutron star mass distribution. *Phys. Rev. Lett.* **73**, 1878–1881 (1994).
7. Thorsett, S. E. & Chakrabarty, D. Neutron Star Mass Measurements. I. Radio Pulsars. *Astrophys. J.* **512**, 288–299 (1999).
8. Taylor, J. H., Fowler, L. A. & McCulloch, P. M. Measurements of general relativistic effects in the binary pulsar PSR1913 + 16. *Nat.* **277**, 437–440 (1979).
9. Taylor, J. H., Wolszczan, A., Damour, T. & Weisberg, J. M. Experimental constraints on strong-field relativistic gravity. *Nat.* **355**, 132–136 (1992).

10. Demorest, P. B., Pennucci, T., Ransom, S. M., Roberts, M. S. E. & Hessels, J. W. T. A two-solar-mass neutron star measured using Shapiro delay. *Nat.* **467**, 1081–1083 (2010).
11. Antoniadis, J. *et al.* A Massive Pulsar in a Compact Relativistic Binary. *Science* **340**, 448 (2013).
12. Valentim, R., Rangel, E. & Horvath, J. E. On the mass distribution of neutron stars. *Mon. Not. R. Astron. Soc.* **414**, 1427–1431 (2011).
13. Özel, F., Psaltis, D., Narayan, R. & Santos Villarreal, A. On the Mass Distribution and Birth Masses of Neutron Stars. *Astrophys. J.* **757**, 55 (2012).
14. Kiziltan, B., Kottas, A., De Yoreo, M. & Thorsett, S. E. The Neutron Star Mass Distribution. *Astrophys. J.* **778**, 66 (2013).
15. Antoniadis, J. *et al.* The millisecond pulsar mass distribution: Evidence for bimodality and constraints on the maximum neutron star mass. *arXiv e-prints* arXiv:1605.01665 (2016).
16. Alsing, J., Silva, H. O. & Berti, E. Evidence for a maximum mass cut-off in the neutron star mass distribution and constraints on the equation of state. *Mon. Not. R. Astron. Soc.* **478**, 1377–1391 (2018).
17. Horvath, J. E. & Valentim, R. The Masses of Neutron Stars. In Alsabti, A. W. & Murdin, P. (eds.) *Handbook of Supernovae*, 1317 (2017).

18. Timmes, F. X., Woosley, S. E. & Weaver, T. A. The Neutron Star and Black Hole Initial Mass Function. *Astrophys. J.* **457**, 834 (1996).
19. Schwab, J., Podsiadlowski, P. & Rappaport, S. Further Evidence for the Bimodal Distribution of Neutron-star Masses. *Astrophys. J.* **719**, 722–727 (2010).
20. Sukhbold, T. & Woosley, S. E. The Compactness of Presupernova Stellar Cores. *Astrophys. J.* **783**, 10 (2014).
21. Müller, B., Heger, A., Liptai, D. & Cameron, J. B. A simple approach to the supernova progenitor-explosion connection. *Mon. Not. R. Astron. Soc.* **460**, 742–764 (2016).
22. Ertl, T., Janka, H. -Th., Woosley, S. E., Sukhbold, T. & Ugliano, M. A Two-parameter Criterion for Classifying the Explodability of Massive Stars by the Neutrino-driven Mechanism. *Astrophys. J.* **818**, 124 (2016).
23. Sukhbold, T., Woosley, S. E. & Heger, A. A High-resolution Study of Presupernova Core Structure. *Astrophys. J.* **860**, 93 (2018).
24. Alpar, M. A., Cheng, A. F., Ruderman, M. A. & Shaham, J. A new class of radio pulsars. *Nat.* **300**, 728–730 (1982).
25. Radhakrishnan, V. & Srinivasan, G. On the origin of the recently discovered ultra-rapid pulsar. *Current Science* **51**, 1096–1099 (1982).

26. Bhattacharya, D. & van den Heuvel, E. P. J. Formation and evolution of binary and millisecond radio pulsars. *Phys. Rep.* **203**, 1–124 (1991).
27. Tauris, T. M., Langer, N. & Kramer, M. Formation of millisecond pulsars with CO white dwarf companions - II. Accretion, spin-up, true ages and comparison to MSPs with He white dwarf companions. *Mon. Not. R. Astron. Soc.* **425**, 1601–1627 (2012).
28. Li, Z., Chen, X., Chen, H.-L. & Han, Z. The Maximum Accreted Mass of Recycled Pulsars. *Astrophys. J.* **922**, 158 (2021).
29. Woosley, S. E., Sukhbold, T. & Janka, H. T. The Birth Function for Black Holes and Neutron Stars in Close Binaries. *Astrophys. J.* **896**, 56 (2020).
30. Lipunov, V. M. & Postnov, K. A. Accretion spin-up of low-magnetic neutron stars. *Astrophys. and Space Sci.* **106**, 103–115 (1984).
31. Talbot, C. & Thrane, E. Measuring the Binary Black Hole Mass Spectrum with an Astrophysically Motivated Parameterization. *Astrophys. J.* **856**, 173 (2018).
32. Woosley, S. E. & Heger, A. The Remarkable Deaths of 9-11 Solar Mass Stars. *Astrophys. J.* **810**, 34 (2015).
33. Hüdepohl, L., Müller, B., Janka, H. T., Marek, A. & Raffelt, G. G. Neutrino Signal of Electron-Capture Supernovae from Core Collapse to Cooling. *Phys. Rev. Lett.* **104**, 251101 (2010).

34. Kresse, D., Ertl, T. & Janka, H.-T. Stellar Collapse Diversity and the Diffuse Supernova Neutrino Background. *Astrophys. J.* **909**, 169 (2021).
35. Ertl, T., Woosley, S. E., Sukhbold, T. & Janka, H. T. The Explosion of Helium Stars Evolved with Mass Loss. *Astrophys. J.* **890**, 51 (2020).
36. Sukhbold, T., Ertl, T., Woosley, S. E., Brown, J. M. & Janka, H. T. Core-collapse Supernovae from 9 to 120 Solar Masses Based on Neutrino-powered Explosions. *Astrophys. J.* **821**, 38 (2016).
37. Evans, M. *et al.* A horizon study for cosmic explorer: Science, observatories, and community. *arXiv:2109.09882 [astro-ph.IM]* (2021).
38. Srivastava, V. *et al.* Science-driven tunable design of cosmic explorer detectors. *The Astrophysical Journal* **931**, 22 (2022).
39. Martynov, D. *et al.* Exploring the sensitivity of gravitational wave detectors to neutron star physics. *Phys. Rev. D* **99**, 102004 (2019).
40. Takami, K., Rezzolla, L. & Baiotti, L. Spectral properties of the post-merger gravitational-wave signal from binary neutron stars. *Phys. Rev. D* **91**, 064001 (2015).
41. Rezzolla, L. & Takami, K. Gravitational-wave signal from binary neutron stars: A systematic analysis of the spectral properties. *Phys. Rev. D* **93**, 124051 (2016).

42. Bauswein, A. *et al.* Identifying a first-order phase transition in neutron-star mergers through gravitational waves. *Phys. Rev. Lett.* **122**, 061102 (2019).
43. Shibata, M. & Taniguchi, K. Merger of binary neutron stars to a black hole: Disk mass, short gamma-ray bursts, and quasinormal mode ringing. *Phys. Rev. D* **73**, 064027 (2006).
44. Baiotti, L., Giacomazzo, B. & Rezzolla, L. Accurate evolutions of inspiralling neutron-star binaries: Prompt and delayed collapse to a black hole. *Phys. Rev. D* **78**, 084033 (2008).

## Methods

### A Mass measurements of neutron stars

Extended Data Tables 1 and 2 list measurements of the mass of 90 neutron stars compiled from the literature. These include 13 double neutron star systems, 27 neutron star and white dwarf binaries, three neutron star and main sequence star binaries, 12 “spider” binary pulsar systems (six redback and six black widow binaries), one isolated neutron star, 14 X-ray binaries (11 high-mass and three low-mass X-ray binaries), five gravitational-wave events of compact binary mergers (two binary neutron star and three neutron star and black hole systems).

A key aspect of this work is that we divided neutron stars into two subclasses: recycled and non-recycled (slow) neutron stars. For most neutron stars, the classification is based on measured spin properties; recycled neutron stars have period  $P \lesssim 100$  ms and  $\dot{P} \lesssim 10^{-17}$ , whereas slow neutron stars have spin periods of the order of seconds or longer. For the latter, no notable accretion-induced spin-up has yet occurred. Moreover, we made the following general assumptions. First, for double neutron star systems and binary neutron star mergers, we assumed that each consists of a recycled and a slow neutron star, with masses  $m_r$  and  $m_s$ , based on the standard formation theory as represented by the double pulsar system PSR J0737–3039A/B<sup>45</sup>. Second, neutron stars in high-mass X-ray binaries are considered to be slow neutron stars; these are neutron stars in the early stage of the recycling process and our assumption is effectively that the amount of accreted mass is negligible. Third, we assumed that neutron stars in neutron star and black hole mergers are non-recycled. This is believed to be the prevailing scenario in which the neutron star is the second object formed in the standard isolated binary formation channel<sup>46,47</sup>.

Our division results in 56 recycled neutron stars and 34 slow neutron stars. For the two recycled neutron stars in GW170817 and GW190425, and the unseen companion of PSR J1906+0746 (assumed to be a recycled neutron star), neither  $P$  nor  $\dot{P}$  have been measured. Therefore, we did not include these three  $m_r$  measurements when accounting for the accreted mass in inferring their birth masses. PSRs J0514–4002A, B2127+11C and J1807–2500B are in globular clusters, which means that they may have originated from a different dynamical formation channel<sup>48–51</sup>. Nevertheless, we included their companions in the category of slow neutron stars (which is a possibility even for the non-standard dynamical formation channel). Third, it was argued that the companion of PSR J0453+1559 could be a white dwarf born in a thermonuclear electron-capture supernova<sup>52</sup>. We do not expect our analysis results to be substantially affected by the inclusion of these four  $m_s$  measurements (companions for three globular-cluster pulsars and PSR J0453+1559).

The input for our hierarchical Bayesian analysis (described in Section C in Methods) are individual mass posteriors. For mass measurements reported with symmetric errors in original publications, they are approximated by Gaussian functions; for gravitational-wave events, we

used posterior samples that are publicly available in the relevant publications<sup>53–57</sup>.

## B Modelling the accreted masses of recycled pulsars

In this section, we describe our methodology for modelling the accreted mass of a recycled pulsar. Our starting point is the measured properties of recycled pulsars, including the spin period, spin-down rate and mass. The goal is to estimate the accreted mass gained in the recycling process and hence estimate the birth masses for each of these pulsars. Our method involves an analytical approach described in the first part of Section B. To fully account for the incomplete understanding of the recycling process, we also consider a phenomenological model as detailed in the second part of Section B. As mentioned in Section A, we aimed to estimate the birth masses of 53 recycled neutron stars. They are placed in two groups: group *a* was composed of all recycled pulsars listed in Extended Data Table 1 as well as the isolated millisecond pulsar J0030+0451 and PSR J1903+0327; group *b* consists of 12 “spider” pulsars, and two recycled neutron stars in low-mass X-ray binaries. It is generally thought that the pulsars in group *a* may have experienced notable spin-down since the end of the recycling process, whereas the pulsars in group *b* probably completed accretion not long before<sup>1</sup>.

In the standard binary-recycling paradigm, recycled pulsars start their post-recycling evolution on a spin-up line, defined as  $\dot{P} \propto P^{4/3}$ , in the  $P$  versus  $\dot{P}$  diagram<sup>27,109</sup>. The exact location of such a spin-up line depends on pulsar-specific properties such as mass, moment of inertia and magnetic inclination angle. For a population of millisecond pulsars, strong observational evidence was recently found for a spin-up line<sup>110</sup>. All pulsars were located to the lower right of this line in the  $P$ - $\dot{P}$  diagram. For pulsars in group *a*, we accounted for the pulsar spin-down evolution by speculating where their spin-up lines might lie in the  $P$ - $\dot{P}$  diagram. For group *b*, we assumed that the spin-down since the end of the recycling process is negligible and, therefore, that the accreted mass is linearly correlated with the *observed* spin period.

The pulsar spin-down evolution can be described in a generic model  $\dot{P} \propto P^{2-n}$ , where  $n$  is the braking index. If magnetic dipole radiation is solely responsible for pulsar spin down, then  $n = 3$ . Observationally, the braking index can be determined from  $n = 2 - (P\ddot{P})/\dot{P}^2$  with  $\ddot{P}$  being the measured second derivative of the spin period. At present, the braking index has been measured only for a handful of normal pulsars<sup>111</sup>, with measured values ranging from 0.9 to 3.15. One theory for  $n$  deviating from 3 is the magnetic field decay, which could occur for isolated young (normal) pulsars<sup>112</sup>. As magnetic field decay is unlikely for (old) recycled pulsars<sup>113</sup>, we adopted the standard<sup>2</sup> value of  $n = 3$ .

<sup>1</sup>The transitional millisecond pulsar J1023+0038 is an excellent example. Its optical variability indicates that it had an accretion disk in 2001<sup>107,108</sup>.

<sup>2</sup>We verified that our results are not sensitive to the adopted value of  $n$ . For example, results with  $n = 2$  are essentially the same.

Extended Data Table 1: **Mass measurements of neutron stars in double neutron star and neutron star-white dwarf systems.** Listed here are pulsar name, the mass of recycled neutron star ( $m_r$ ), slow neutron star ( $m_s$ ) and companion star ( $m_c$ ), spin period ( $P$ ), the intrinsic spin-down rate ( $\dot{P}$ ), orbital period ( $P_b$ ) and eccentricity ( $e_0$ ). Mass uncertainties are quoted in parentheses.

Pulsar Name	$m_r$ ( $M_\odot$ )	$m_s$ ( $M_\odot$ )	$m_c$ ( $M_\odot$ )	$P$ (ms)	$\dot{P}$ ( $10^{-18}$ )	$P_b$ (day)	$e_0$	Reference
Double neutron star systems								
J0514–4002A	1.25(6)	1.22(6)	–	4.99	0.084	18.785	0.888	58
J1829+2456	1.306(4)	1.299(4)	–	41.01	0.0435	1.176	0.139	59
J1906+0746	1.322(11)	1.291(11)	–	144.1	20268	0.166	0.085	60
B1534+12	1.3330(2)	1.3455(2)	–	37.90	2.364	0.421	0.274	61
J0737–3039A	1.3381(7)	1.2489(7)	–	22.70	1.761	0.102	0.088	62
J0509+3801	1.34(8)	1.46(8)	–	76.54	7.924	0.380	0.586	63
J1757–1854	1.3406(5)	1.3922(5)	–	21.50	2.654	0.184	0.606	64
J1756–2251	1.341(7)	1.230(7)	–	28.46	1.015	0.320	0.181	65
B2127+11C	1.358(10)	1.354(10)	–	30.53	5.01	0.335	0.681	66
J1807–2500B	1.3655(21)	1.2064(21)	–	4.19	0.113	9.957	0.747	67
B1913+16	1.4398(2)	1.3886(2)	–	59.03	8.645	0.323	0.617	68
J0453+1559	1.559(5)	1.174(4)	–	45.78	0.177	4.072	0.113	69
J1913+1102	1.62(3)	1.27(3)	–	27.29	0.176	0.206	0.090	70
Neutron star-white dwarf systems								
J1802–2124	1.24(11)	–	0.78	12.65	0.071	0.699	$10^{-6}$	71
J2045+3633	1.251(21)	–	0.873	31.68	0.594	32.30	0.017	72
J1141–6545	–	1.27(1)	1.01	393.9	4295	0.198	0.172	73
J1918–0642	1.29(10)	–	0.231	7.646	0.024	10.91	$10^{-5}$	74
J1910–5959A	1.33(11)	–	0.18	3.266	0.0056	0.837	$10^{-6}$	75
J1949+3106	1.34(17)	–	0.81	13.14	0.094	1.95	$10^{-5}$	76
J1713+0747	1.35(7)	–	0.292	4.57	0.008	67.83	$10^{-4}$	74
J2234+0611	1.353(17)	–	0.298	3.577	0.006	32.0	0.129	77
J2305+4707	–	1.38(10)	1.26	1066	569	12.34	0.658	7,78
J2043+1711	1.38(13)	–	0.173	2.38	0.004	1.48	$10^{-6}$	74
J2053+4650	1.40(21)	–	0.86	12.59	0.166	2.45	$10^{-5}$	79
J0337+1715	1.4359(3)	–	0.1973	2.733	0.017	1.629	$10^{-3}$	80
J0437–4715	1.44(7)	–	0.224	5.76	0.014	5.74	$10^{-5}$	81
J1738+0333	1.47(7)	–	0.181	5.85	0.022	0.355	$10^{-7}$	82
J1909–3744	1.486(11)	–	0.208	2.95	0.0027	1.533	$10^{-7}$	83
J1950+2414	1.496(23)	–	0.28	4.30	0.020	22.19	0.08	76
J1125–6014	1.5(2)	–	0.31	2.63	0.002	8.753	$10^{-6}$	83
J1857+0943	1.54(13)	–	0.263	5.36	0.017	12.327	$10^{-5}$	83
J0751+1807	1.64(15)	–	0.16	3.48	0.006	0.263	$10^{-6}$	84
J0955–6150	1.71(3)	–	0.254	2.0	0.15	24.58	0.118	85
J1012+5307	1.72(16)	–	0.165	5.26	0.011	0.605	$10^{-6}$	86
J1600–3053	1.77(36)	–	0.34	3.598	0.009	14.35	$10^{-3}$	83
J1946+3417	1.828(22)	–	0.2556	3.17	0.003	27.02	0.134	87
J2222–0137	1.831(10)	–	1.319	32.82	0.017	2.446	$10^{-3}$	88
J1614–2230	1.908(16)	–	0.493	3.15	0.0096	8.687	$10^{-6}$	74
J0348+0432	2.01(4)	–	0.172	39.12	0.241	0.102	$10^{-6}$	11
J0740+6620	2.08(7)	–	0.253	2.89	0.0054	4.77	$10^{-6}$	89

Extended Data Table 2: **Mass measurements of neutron stars in other types of systems.** Entries filled with a dash line are inapplicable, while leaving blank indicates an unknown parameter. Error ranges for gravitational wave events represent  $1\sigma$  errors.

Name	$m_r (M_\odot)$	$m_s (M_\odot)$	$m_c (M_\odot)$	$P$ (ms)	$\dot{P} (10^{-18})$	$P_b$ (day)	Reference
Neutron star plus main-sequence star systems							
LAMOST J1123	–	1.24(3)	0.61			0.274	90
PSR J0045–7319	–	1.58(34)	10	926.3	4463	51.17	74
PSR J1903+0327	1.666(12)	–	1.033	2.15	0.0188	95.17	7
Redback binary pulsar systems							
PSR J1723–2837	1.22(26)	–	0.36	1.856	0.008	0.615	91
PSR J2039–5617	1.3(1)	–	0.2	2.651	0.014	0.228	92
PSR J2339–0533	1.64(27)	–	0.35	2.884	0.014	0.193	91
PSR J1023+0038	1.71(16)	–	0.24	1.688	0.0053	0.198	93
PSR J2129–0429	1.74(18)	–	0.44	7.62		0.635	94
PSR J2215+5135	2.28(10)	–	0.25	2.610	0.0334	0.173	95
Black widow binary pulsar systems							
PSR J1555–2908	1.67(7)	–	0.06	1.788	0.045	0.234	96
PSR J1301+0833	1.74(20)	–	0.035	1.84		0.27	97
PSR J1810+1744	2.13(4)	–	0.065	1.66		0.15	98
PSR J1653–0158	2.17(21)	–	0.014	1.968	0.0008	0.052	99
PSR J1959+2048	2.18(9)	–	0.033	1.607	0.0169	0.382	95
PSR J0952–0607	2.35(17)	–	0.032	1.41	0.0046	0.268	100
Isolated neutron stars							
PSR J0030+0451	1.44(15)	–	–	4.865	0.010	–	101, 102
Low-mass X-ray binaries							
4U 1608–52	1.57(30)	–		1.61		0.537	103
KS 1731–260	1.61(37)	–		1.91			103
X1822–371	–	1.69(13)	0.46	590		0.232	104
High-mass X-ray binaries (spin periods in seconds)							
4U 1538–522	–	1.02(17)	16	526.8		3.728	104
SMC X–1	–	1.21(12)	18	0.71		3.892	105
XTE J1855–026	–	1.41(24)	21	360.7		6.074	105
LMC X–4	–	1.57(11)	18	13.5		1.408	105
Cen X–3	–	1.57(16)	24	4.8		2.087	105
SAX J1802.7–2017	–	1.57(25)	22	139.6		4.570	105
OA0 1657–415	–	1.74(30)	17.5	37.3		10.447	105
EXO 1722–363	–	1.91(45)	18	413.9		9.741	105
4U 1700–377	–	1.96(19)	46			3.412	105
J013236.7+303228	–	2.0(4)	11			1.73	106
Vela X–1	–	2.12(16)	26	283.2		8.964	105
Binary neutron star mergers							
GW170817	$1.34^{+0.12}_{-0.09}$	$1.38^{+0.11}_{-0.11}$	–				53, 55
GW190425	$1.64^{+0.13}_{-0.11}$	$1.66^{+0.12}_{-0.12}$	–				54, 55
Neutron star-black hole mergers							
GW191219	–	$1.17^{+0.07}_{-0.06}$	31.1				57
GW200115	–	$1.4^{+0.6}_{-0.2}$	5.9				56
GW200105	–	$1.9^{+0.2}_{-0.2}$	8.9				56

A magnetized neutron star accreting matter from a companion star may reach an equilibrium spin period  $P_{\text{eq}}$  that is given by the Keplerian orbital period at the inner edge of the accretion disk:

$$P_{\text{eq}} = 2\pi \sqrt{\frac{r_{\text{mag}}^3}{Gm} \frac{1}{\omega_c}}, \quad (1)$$

where  $G$  is the gravitational constant,  $m$  is pulsar mass, and  $0.25 < \omega_c \leq 1$  is the critical fastness parameter<sup>109</sup>. The inner radius of the accretion disk  $r_{\text{mag}} = \phi r_A$ , with  $r_A$  being the Alfvén radius, which is a characteristic radius at which magnetic stresses dominate the matter flow in the accretion disk:

$$r_A \approx \left( \frac{B^2 R^6}{\dot{M} \sqrt{2Gm}} \right)^{2/7}, \quad (2)$$

where  $B$  is the magnetic field strength,  $R$  is the pulsar radius and  $\dot{M}$  is the accretion rate. The parameter  $\phi$  is generally assumed to be in the range between 0.5 and 1.4, depending on the poorly known disk-magnetosphere interactions<sup>109</sup>.

The field strength of a magnetic dipole can be estimated as<sup>114</sup>

$$B = \sqrt{\frac{c^3 I P \dot{P}}{4\pi^2 R^6} \frac{1}{1 + \sin^2 \alpha}}, \quad (3)$$

where  $c$  is the speed of light,  $I$  is the pulsar moment of inertia and  $\alpha$  is the misalignment angle between the magnetic dipole moment and the spin axis. Note that Equation (3) is a convenient approximation of numerical results in ref.<sup>114</sup>, which takes into account the plasma contribution in the spin-down torque. Inspecting Equations (1-3), one finds that  $\dot{P} = AP^{4/3}$ , with the coefficient  $A$  given by<sup>27</sup>

$$A = \frac{2^{1/6} G^{5/3} \dot{M} m^{5/3}}{\pi^{1/3} c^3} \frac{1}{I} (1 + \sin^2 \alpha) \phi^{-7/2} \omega_c^{7/3}. \quad (4)$$

As can be seen from Equation (4), the spin-up line is not uniquely defined. Instead, the coefficient  $A$  depends on pulsar-specific parameters. In this work, we adopt  $A = A_{\text{max}} = 3.76 \times 10^{-15} \text{ s}^{-4/3}$  as the upper limit for the population of recycled pulsars<sup>110</sup>. We also adopted the following empirical relation for the moment of inertia<sup>115</sup>

$$I \approx 0.237 m R^2 \left[ 1 + 4.2 \frac{m}{M_\odot} \frac{\text{km}}{R} + 90 \left( \frac{m}{M_\odot} \frac{[\text{km}]}{R} \right)^4 \right]. \quad (5)$$

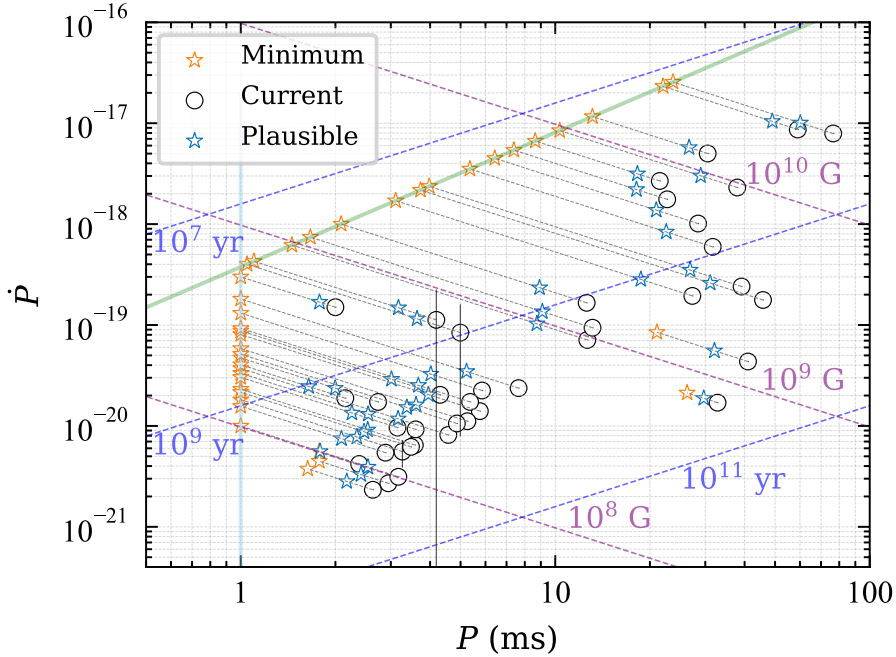
The intersection between the spin-down line  $\dot{P} \propto P^{2-n}$  and the limiting spin-up line (with  $A = A_{\text{max}}$ ) gives a minimum initial spin period for recycled pulsars. However, for some pulsars this minimum period (determined from the intersection of two lines) was unphysically small, in

which case we set the minimum spin period to 1 ms. This is close to the break-up spin period of neutron stars<sup>116</sup>. Also note that in a recent numerical simulation study, the spin period of a neutron star at the end of the recycling process was found to be  $\gtrsim 1$  ms for a range of binary evolution calculations<sup>28</sup>. The time spent for a pulsar to evolve from an initial spin period ( $P_0$ ) to its current location in the  $P$ - $\dot{P}$  diagram is

$$\tau = \frac{P}{(n-1)\dot{P}} \left[ 1 - \left( \frac{P_0}{P} \right)^{n-1} \right]. \quad (6)$$

Here if  $P_0 \ll P$  and  $n = 3$ , this reduces to the expression for the characteristic age ( $\tau_c$ ). We denote the time for a pulsar to evolve from either the spin-up line or  $P_0 = 1$  ms to its current period as the maximum age  $\tau_{\max}$ . If  $\tau_{\max}$  is greater than the age of Milky Way, 11 Gyr (refs. <sup>117,118</sup>), we set it to 11 Gyr.

In our calculations, we first obtained pulsar intrinsic spin-down rate  $\dot{P}_{\text{int}}$  by correcting the measured  $\dot{P}$  with contribution from the Shklovskii effect<sup>119</sup> and Galactic potential<sup>120,121</sup> using the package `GalDynPsr`<sup>122</sup>. For three pulsars in globular clusters, PSRs J1910–5959A, B2127+11C and J1807–2500B, the contribution from cluster potential was also included<sup>123</sup>.



**Extended Data Figure 1 The pulsar  $P$ - $\dot{P}$  diagram for 39 recycled pulsars.** Black circles mark their current locations (where the error bars on the intrinsic  $\dot{P}$  are too small to be seen except for the two globular-cluster pulsars), whereas orange and blue stars mark the minimum and plausible initial spin periods (assuming a braking index  $n = 3$ ), respectively. The solid green line is the limiting spin-up line  $\dot{P} \propto P^{4/3}$  inferred for the

population of millisecond pulsars<sup>110</sup>.

Extended Data Figure 1 shows the locations of 39 recycled pulsars (in group *a*) in the  $P$ - $\dot{P}$  diagram. Their observed locations with intrinsic  $\dot{P}_{\text{int}}$  are marked by black circles. Orange stars indicate the minimum spin period  $P_{\text{lim}}$  and its corresponding initial spin-down rate  $\dot{P}_{\text{lim}}$ . For a braking index of 3, black dotted lines ( $\dot{P} \propto P^{-1}$ ) connect the black circles and orange stars. Note that  $P_{\text{lim}}$  and  $\dot{P}_{\text{lim}}$  are determined by three constraints: the limiting spin-up line (green line in Extended Data Figure 1), a minimum spin period of 1 ms (a vertical blue line), and a maximum age of 11 Gyr. For orange stars that do not fall onto the green or blue lines, their locations are a result of the age limit. Light blue stars in this plot indicate plausible places of recycled pulsars at the end of recycling process. As we assumed that the age of a recycled pulsar is uniformly distributed in  $[0, \tau_{\text{max}}]$ , blue stars correspond to an age of  $\tau_{\text{max}}/2$ .

**An analytical model** In our analytical model, we approximate the equilibrium spin period of a neutron star at the end of the recycling process as the minimum spin period accelerated from rest<sup>30</sup>:

$$P_{\text{eq}} = \frac{3\pi I}{\sqrt{Gr_{\text{mag}}}} \left( m^{3/2} - m_{\text{ini}}^{3/2} \right)^{-1}, \quad (7)$$

where  $m_{\text{ini}} = m - \Delta m$  is the neutron-star mass before accretion (its birth mass),  $m$  is the measured neutron-star mass and  $\Delta m$  is the accreted mass that is being modelled here.

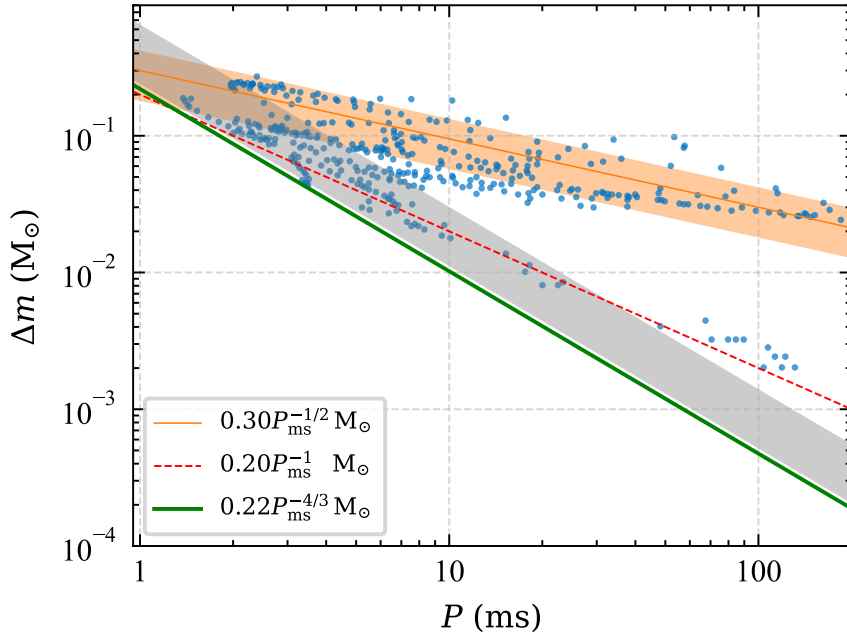
From Equations (1)-(5) and (7), it can be seen that, the spin-up line and the accreted mass is uniquely determined for a given set of parameters  $\{\dot{M}, \alpha, R, \phi, \omega_c\}$ , if we assume that a recycled pulsar starts its rejuvenated life from the spin-up line and spins down due to magnetic dipole braking. Therefore, we modelled  $\Delta m$  in a parameter-agnostic way. For each recycled pulsar, we set the following priors on its recycling parameters. The accretion rate, when expressed in units of the Eddington accretion rate, follows a log-uniform distribution between 0.01 and 3. The upper end was chosen to allow for possible super-Eddington accretion<sup>124</sup>. The magnetic inclination angle  $\alpha$  is distributed isotropically, with  $\cos \alpha$  uniform between  $-1$  and  $1$ . The dimensionless parameters  $\phi$  and  $\omega_c$  are uniformly distributed in the ranges  $[0.5, 1.4]$  and  $[0.25, 1]$ , respectively. The pulsar radius follows a Gaussian distribution with a mean of 11.9 km and a standard deviation of 0.85 km, based on gravitational-wave observations of the first neutron star merger GW170817<sup>125</sup>. We have verified that the effect of using a mass-radius relation for a specific equation of state that is consistent with current observational constraints, for example, the AP4 equation of state<sup>126</sup>, is of the order of  $\lesssim 10\%$ .

For each pulsar, we generated a sample in the six-dimensional parameter space  $\{m, \dot{M}, \alpha, R, \phi, \omega_c\}$ , and draw a spin-up line (which must lie to the upper left of the current location of pulsar in the  $P$ - $\dot{P}$  diagram). Then, the intersection between this spin-up line and the constant magnetic field strength line  $\dot{P} \propto P^{-1}$  determines an equilibrium spin period  $P_{\text{eq}}$ . The accreted mass  $\Delta m$  was then computed from Equation (7). Note that the statistical uncertainties of  $P$  and  $\dot{P}$  were ignored, which is an excellent approximation for all pulsars except one globular-cluster

pulsar.

For recycled neutron stars in group *b*, we adopted a simple scaling relation (plotted as the red dashed line in Extended Data Figure 2) between the accreted mass  $\Delta m$  and the observed spin period:  $\Delta m/M_\odot = 0.2P_{\text{ms}}^{-1}$  where  $P_{\text{ms}}$  is the spin period in milliseconds; see, for example, equation (6) in ref. <sup>127</sup>. Such a relation can be obtained from Equation (7) when  $\Delta m \ll m$ .

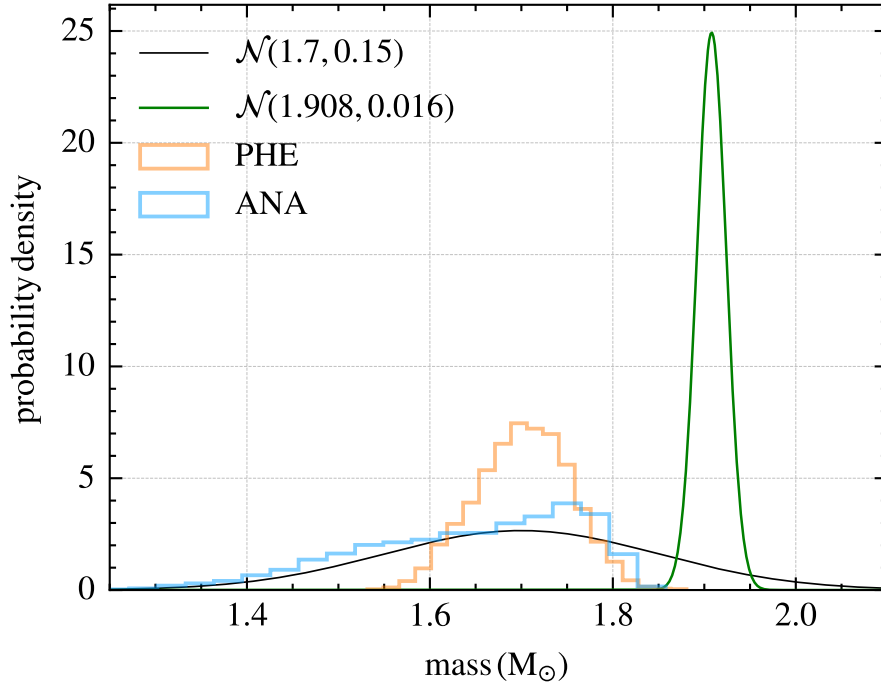
**A phenomenological model** Here we estimate the accreted masses of recycled neutron stars using a phenomenological relation between  $\Delta m$  and the initial spin periods  $P_{\text{ini}}$ . As in the analytic model, for group *b* neutron stars, we assumed that the observed spin periods are their initial spin periods. For group *a* pulsars, the initial spin period was determined as follows. We assumed that the true age of a recycled pulsar is uniformly drawn from  $[0, \tau_{\text{max}}]$ . For a given true age, we evolved the pulsar back in time following the spin-down equation  $\dot{P} \propto P^{2-n}$  to find its  $P_{\text{ini}}$ . We generated  $10^4$  random ages uniformly drawn from  $[0, \tau_{\text{max}}]$  and obtained the distribution of initial spin periods  $P_{\text{ini}}$ . For a given  $P_{\text{ini}}$ ,  $\Delta m$  is drawn from a Gaussian distribution with a mean of  $\mu_M/M_\odot = 0.3P_{\text{ms}}^{-1/2}$  (with  $P_{\text{ms}}$  being the initial spin period measured in milliseconds) and a standard deviation of  $0.2\mu_M$ . The mean in this recipe is motivated by numerical simulations that take into account the neutron star spin-down due to propeller effects during the recycling process<sup>28</sup>; see the blue dots Extended Data Figure 2. The 20% dispersion is the typical spread found in the analytical prescription.



**Extended Data Figure 2** The accreted mass-spin period ( $\Delta m$ - $P$ ) correlation used to correct for mass accreted by recycled pulsars. The green solid line depicts a lower limit on the accreted mass<sup>24,27</sup>, while the orange solid lines and shaded

band represent the mean and 90% credible region of our phenomenological model. The red dashed line is a simple scaling used in the literature<sup>30,127</sup>. The grey shaded band encompasses 90% credible region of our analytical model. Blue dots are from numerical simulations of the recycling process performed in ref.<sup>28</sup>.

Extended Data Figure 2 illustrates our prescriptions for the accreted mass-spin period correlation. The green and orange solid lines represent  $\Delta m_{\min}/M_{\odot} = 0.22P_{\text{ms}}^{-4/3}$  and  $\mu_M/M_{\odot} = 0.3P_{\text{ms}}^{-1/2}$ , respectively. The grey- and orange-shaded bands encompass the 90% credible regions of the analytical and phenomenological models, respectively. The red dashed line is  $\Delta m/M_{\odot} = 0.2P_{\text{ms}}^{-1}$ . Results from numerical simulations of the recycling process in ref.<sup>28</sup> are marked as blue dots. Note that their calculations were performed for a fiducial value of the initial magnetic field strength and neutron star moment of inertia. Our models captures the overall trend and scatter of the numerical results well. The difference between grey and orange bands for  $P \gtrsim 10$  ms is exaggerated due to the logarithmic scale of the vertical coordinate in Extended Data Figure 2.



**Extended Data Figure 3 The mass probability distribution of PSR J1614–2230.** The green curve depicts the measured mass<sup>74</sup>, whereas the black curve is the birth mass deduced from detailed binary evolution calculations<sup>128</sup>, based on the original measured mass of  $1.97 \pm 0.04 M_{\odot}$ <sup>10</sup>. Birth masses estimated from our analytical and phenomenological models are shown in blue and orange, respectively.

**A case study of PSR J1614–2230.** PSR J1614–2230, which has an observed spin period of 3.15 ms, was the first binary pulsar found to have a measured neutron-star mass around  $2 M_{\odot}$ . The pulsar mass was originally measured as  $1.97 \pm 0.04 M_{\odot}$ , and the neutron star is in an 8.7-day orbit with a  $0.5 M_{\odot}$  white dwarf companion<sup>10</sup>. By performing detailed binary evolution calculations, Tauris et al.<sup>128</sup> suggested that the most probable progenitor system of PSR J1614–2230 is a  $1.7 \pm 0.15 M_{\odot}$  neutron star going through “case A” Roche lobe overflow (and, thus, accreting mass) from an  $\sim 4.5 M_{\odot}$  donor star. An independent binary evolution study found a *minimum* initial (birth) mass of  $1.6 \pm 0.1 M_{\odot}$  (ref.<sup>129</sup>).

The mass measurement of PSR J1614–2230 was updated in 2018 to a slightly lower value of  $1.908 \pm 0.016 M_{\odot}$  with extended observations<sup>74</sup>. From our accreted-mass modelling, we found that its birth mass was around  $1.7 M_{\odot}$ , in excellent agreement with binary evolution calculations. Extended Data Figure 3 shows the measured and inferred birth-mass distributions of PSR J1614–2230. The blue and orange curves indicate the birth masses estimated from our analytical and phenomenological modelling, respectively.

## C Bayesian inference

In this section, we briefly describe the method of Bayesian inference used to determine the birth-mass function of neutron stars; a more general introduction can be found in refs.<sup>130,131</sup>.

The data analyzed are posterior distributions for 90 neutron stars. The original dataset, denoted as OBS, consists of Gaussian mass posteriors used to approximate measurements reported in the literature (as summarized in Extended Data Tables 1 and 2) or posterior samples, if available. For 53 of the recycled pulsars in our compilation, we also applied probabilistic accreted mass corrections to obtain posteriors for their birth masses. The dataset obtained with the analytical (phenomenological) prescription described in Section B is denoted as ANA (PHE). A dataset that includes only those measurements of slow (non-recycled) neutron stars is denoted as SLOW. For comparison, the dataset that includes only observed masses of 53 recycled pulsars is denoted as REC. The ANA<sub>m<sub>r</sub></sub> (PHE<sub>m<sub>r</sub></sub>) dataset includes the birth masses of 53 recycled pulsars only after applying the analytical (phenomenological) accreted-mass correction. The ANA<sub>radio</sub> dataset is a subset of ANA that includes only mass measurements obtained by the radio pulsar timing method (i.e., all in Extended Data Table 1, plus PSR J1903+0327).

Let  $p(m^i|d^i)$  be the mass posterior distribution of the  $i$ th neutron star, given some observations  $d^i$ . Our goal is to find a model that can best describe the collection of mass posteriors for  $N$  sources. We introduce a conditional prior for neutron-star mass  $\pi(m^i|\Lambda)$  for a given model  $M$  that includes hyperparameters  $\Lambda$ . The hyperposterior distribution of  $\Lambda$  can be written as

$$p(\Lambda|\{d\}, M) = \frac{1}{\mathcal{Z}_{\Lambda}(M)} \prod_{i=1}^N \int dm^i \mathcal{L}(d^i|m^i) \pi(m^i|\Lambda) \pi(\Lambda|M), \quad (8)$$

where  $\{d\}$  denotes the original observations that provide individual neutron-star mass measurements,  $\pi(\Lambda|M)$  is the prior distribution for  $\Lambda$  and the term  $\mathcal{L}(d^i|m^i)$  is the likelihood function of the data given  $m^i$ , which is related to the mass posterior through

$$\mathcal{L}(d^i|m^i) = \frac{\mathcal{Z}_0^i}{\pi_0(m^i)} p(m^i|d^i), \quad (9)$$

where  $\pi_0(m^i)$  is the initial prior used to derive the mass posterior (assumed to be flat here) and  $\mathcal{Z}_0^i$  is the initial evidence, which is a factor that will ultimately cancel out through either normalization of the hyperposterior or the construction of a Bayesian evidence ratio.

The term  $\mathcal{Z}_\Lambda(M)$  in Equation (8) is the hyperevidence

$$\mathcal{Z}_\Lambda(M) = \int d\Lambda \prod_{i=1}^N \int dm^i \mathcal{L}(d^i|m^i) \pi(m^i|\Lambda) \pi(\Lambda|M). \quad (10)$$

In practice, we can replace the integral over  $dm^i$  with a summation over the conditional prior at posterior samples of  $m^i$ , so that the hyperevidence is given by

$$\mathcal{Z}_\Lambda(M) = \int d\Lambda \prod_{i=1}^N \frac{\mathcal{Z}_0^i}{n_i} \sum_{k=1}^{n_i} \frac{\pi(m_k^i|\Lambda)}{\pi_0(m_k^i)} \pi(\Lambda|M), \quad (11)$$

where  $n_i$  is the number of mass posterior samples for the  $i$ th neutron star.

To find the model that best fits the birth-mass function of neutron stars, we compute the Bayes factor between two models ( $M_1$  and  $M_2$ ), defined as follows

$$\text{BF}_{M_2}^{M_1} = \frac{\mathcal{Z}_\Lambda(M_1)}{\mathcal{Z}_\Lambda(M_2)}. \quad (12)$$

We followed the interpretation of Bayes factors outlined by ref.<sup>132</sup> and choose a threshold for BF of 150, corresponding to a natural logarithmic BF of 5, as required for confident model selection. Note that the Bayes factor is equal to the odds, which is defined as the ratio of the posterior probabilities between two models, assuming that their prior probabilities are equal.

The likelihood function adopted above is applicable when individual neutron-star mass measurements are independent. For Galactic double neutron star systems, the mass measurements are correlated because of the significant constraint on the total mass of two neutron stars, as demonstrated in figure 1 in ref.<sup>133</sup>. In this case, the joint posteriors of two masses should be used following the formalism outlined in Section 3.1 of ref.<sup>133</sup>. To illustrate this point explicitly, the total likelihood that is hidden in Equation (8) is

$$\mathcal{L}(\{d\}|\Lambda) = \prod_{i=1}^{90} \int dm^i \mathcal{L}(d^i|m^i) \pi(m^i|\Lambda), \quad (13)$$

which should be modified as follows:

$$\prod_{i=1}^{64} \int dm^i \mathcal{L}(d^i|m^i)\pi(m^i|\Lambda) \times \prod_{j=1}^{13} \int dm_1^j dm_2^j \mathcal{L}(d^j|m_1^j, m_2^j)\pi(m_1^j|\Lambda)\pi(m_2^j|\Lambda). \quad (14)$$

We divided the 90 neutron stars into two groups: the first group includes 64 neutron stars whose mass posteriors are truly independent; the second group contains 13 pairs of neutron stars (labelled as  $m_1^j$  and  $m_2^j$ ) that are in double neutron star systems. For the second group, the individual likelihood function  $\mathcal{L}(d^j|m_1^j, m_2^j)$  is proportional to the joint posterior  $p(m_1^j, m_2^j|d^j)$ .

In our analysis, we used the software package `BILBY` (ref. <sup>134</sup>) for parameter estimation and evidence calculation and the `gwpopulation` package <sup>135</sup> for population modelling.

## D Parametric models for the neutron star mass function

In this section, we describe a range of parametric models for  $\pi(m|\Lambda)$  and specify the priors adopted for hyperparameters  $\pi(\Lambda|M)$ .

Our base model is a uniform distribution:

$$\begin{aligned} \pi(m | \Lambda) &= \pi(m | \{m_{\min}, m_{\max}\}) \\ &= \begin{cases} \frac{1}{m_{\max} - m_{\min}} & m_{\min} \leq m \leq m_{\max} \\ 0 & \text{otherwise} \end{cases}, \end{aligned} \quad (15)$$

where  $m_{\min}$  and  $m_{\max}$  are the maximum and minimum neutron-star mass, respectively. For the uniform model and all other models where applicable, we adopted uniform priors in the ranges  $[0.9, 2.9]M_{\odot}$  and  $[1.9, 2.9]M_{\odot}$  for  $m_{\min}$  and  $m_{\max}$ , respectively. The prior edges were chosen to be the same as in ref. <sup>16</sup> to facilitate comparisons.

The probability distribution of a Gaussian model is given by

$$\begin{aligned} \pi(m | \Lambda) &= \pi(m | \{\mu, \sigma\}) \\ &= \frac{1}{\sigma\sqrt{2\pi}} \exp \left[ -\frac{1}{2} \left( \frac{m - \mu}{\sigma} \right)^2 \right], \end{aligned} \quad (16)$$

where  $\mu$  and  $\sigma$  are the mean and standard deviation, respectively. This model can be extended to multi-component Gaussians. As in ref. <sup>16</sup>, we also considered the two-Gaussian (2G) and three-Gaussian (3G) models. For 2G, we have  $\Lambda = \{\mu_1, \sigma_1, \mu_2, \sigma_2, \alpha\}$ , whereas for 3G model,  $\Lambda = \{\mu_1, \sigma_1, \mu_2, \sigma_2, \mu_3, \sigma_3, \alpha, \beta\}$ . Here  $\alpha$  and  $\beta$  are the weights of the first and second Gaussian components, respectively. We adopt uniform priors in the ranges  $[0.9, 2.9]M_{\odot}$  and  $[0.01, 2]M_{\odot}$  for the mean and standard deviation, respectively, with a further constraint of  $\mu_i < \mu_{i+1}$  for

multi-component Gaussian models. The priors for weight parameters  $\alpha$  and  $\beta$  are uniform between 0.01 and 1. For 2G, we also added a minimum-mass ( $m_{\min}$ ) cutoff, a maximum-mass ( $m_{\max}$ ) cutoff or both. These models are denoted as  $2G_{\min}$ ,  $2G^{\max}$ , and  $2G_{\min}^{\max}$ , respectively. In the case with a mass cutoff (truncated Gaussians), the probability distribution is properly normalized.

The probability distribution in the log-Uniform model is

$$\begin{aligned}\pi(m | \Lambda) &= \pi(m | \{m_{\min}, m_{\max}\}) \\ &= \begin{cases} \frac{1}{m \log(m_{\max}/m_{\min})} & m_{\min} \leq m \leq m_{\max} \\ 0 & \text{otherwise} \end{cases},\end{aligned}\quad (17)$$

Whereas the log-Normal distribution is defined as

$$\begin{aligned}\pi(m | \Lambda) &= \pi(m | \{\mu, \sigma\}) \\ &= \frac{1}{\sqrt{2\pi}m\sigma} \exp\left[-\frac{(\log m - \mu)^2}{2\sigma^2}\right].\end{aligned}\quad (18)$$

The prior edges of the log-Normal model are chosen to match those of the Gaussian model.

In the power-law model, the neutron star mass function is given by

$$\begin{aligned}\pi(m | \Lambda) &= \pi(m | \{m_{\min}, m_{\max}, \alpha\}) \\ &= \begin{cases} \frac{1-\alpha}{m_{\max}^{1-\alpha} - m_{\min}^{1-\alpha}} m^{-\alpha} & m_{\min} \leq m \leq m_{\max} \\ 0 & \text{otherwise} \end{cases}.\end{aligned}\quad (19)$$

Here the power-law index takes a uniform prior between  $-5$  and  $25$ . The power-law distribution can be modified to allow a smooth turn-on over a range of  $\delta m$ , which takes a uniform prior between  $0.01$  and  $1M_{\odot}$  in our analysis. Such a TOP model is defined as

$$\begin{aligned}\pi(m | \Lambda) &= \pi(m | \{m_{\min}, m_{\max}, \alpha, \delta m\}) \\ &= m^{-\alpha} S(m, m_{\min}, \delta m) \mathcal{H}(m_{\max} - m),\end{aligned}\quad (20)$$

where  $\mathcal{H}$  is the Heaviside step function and  $S$  denotes a smoothing function, which is designed to rise from 0 at  $m_{\min}$  to 1 at  $(m_{\min} + \delta m)$ . In the interval of  $m_{\min} < m < m_{\min} + \delta m$ , the function  $S$  can be expressed by

$$S(m, m_{\min}, \delta m) = \left[ \exp\left(\frac{\delta m}{m - m_{\min}} + \frac{\delta m}{m - m_{\min} - \delta m}\right) + 1 \right]^{-1}.\quad (21)$$

Note that in plots of the posterior distributions of TOP parameters, we show the parameter  $m_{\text{peak}}$  which defines the peak location of the distribution.

The gamma distribution is defined as

$$\pi(m | \Lambda) = \pi(m | \alpha, \theta) = \frac{m^{(\alpha-1)} \exp\left(-\frac{m}{\theta}\right)}{\theta^\alpha \Gamma(\alpha)}, \quad (22)$$

where  $\Gamma(\alpha)$  is the gamma function, the  $\alpha$  is the shape parameter and  $\theta$  is the scalar parameter. We adopted uniform priors for  $\alpha$  and  $\theta$  in the range of  $(0, 80)$  and  $(0.01, 0.1)$ , respectively.

The skewed Student's  $t$ -distribution (SST) can be parameterized as<sup>136,137</sup>

$$\pi(m | \Lambda) = \pi(m | \mu, \sigma, \nu, \tau) = \begin{cases} \frac{c}{\sigma_0} \left[1 + \frac{\nu^2 z^2}{\tau}\right]^{-(\tau+1)/2} & \text{if } m < \mu_0, \\ \frac{c}{\sigma_0} \left[1 + \frac{z^2}{\nu^2 \tau}\right]^{-(\tau+1)/2} & \text{if } m \geq \mu_0. \end{cases} \quad (23)$$

Here  $\mu$  and  $\sigma$  are the mean and standard deviation of the Gaussian distribution, respectively. The parameters  $\nu$  and  $\tau$  are used to characterize the degree of skewness. In Equation (23),  $\mu_0 = \mu - \sigma\kappa/s$ ,  $\sigma_0 = \sigma/s$ ,  $z = (m - \mu_0)/\sigma_0$ , and  $c = 2\nu [(1 + \nu^2) B(1/2, \tau/2) \tau^{1/2}]^{-1}$  with  $\kappa$  and  $s$  given by  $\kappa = 2\tau^{1/2} (\nu - \nu^{-1}) [(\tau - 1) B(1/2, \tau/2)]^{-1}$  and  $s = \left[\frac{\tau}{(\tau-2)} (\nu^2 + \nu^{-2} - 1) - \kappa^2\right]^{1/2}$ , respectively;  $B$  is the beta function. Priors for  $\mu$  and  $\sigma$  were the same as those of the Gaussian-family models, and we adopted uniform priors for  $\nu$  and  $\tau$  in the ranges  $(0, 8)$  and  $(2, 20)$ , respectively.

## E Further details of analysis results and discussions

Extended Data Table 3 lists the log Bayes factors for 15 models in comparison to the uniform distribution for 9 data sets, including the original observed masses (OBS), the observed masses of double neutron star systems (OBS<sub>DNS</sub>), and accounting for various accreted-mass corrections. One can see that the turn-on power law (TOP) distribution is the best-performing model across 9 different data sets. The TOP model is favoured against the two-Gaussian (2G) model with a natural logarithmic Bayes factor greater than 5 for both the analytical and phenomenological prescriptions of accreted-mass corrections. We consider two additional features in the mass spectrum on top of the TOP model: a maximum-mass cutoff (“TOP<sup>max</sup>”) and a Gaussian peak (denoted as “TOPG”). We find that there is marginal support for a maximum-mass cutoff but no support for a Gaussian peak. For simplicity, in referring to the preferred model from data, we do not distinguish between TOP and TOP<sup>max</sup>.

In order to verify the significance of our results, we simulate a sample of 87 neutron star mass measurements. The mean values of these neutron star masses are drawn from a 2G distribution, with parameters corresponding to the maximum a posteriori probability values inferred from the ANA data set; their measurement uncertainties are the same as the actual data set; here we rank the mean values of both simulated and real neutron star masses, and assign the

measurement uncertainty of actual neutron star mass measurement to its simulated counterpart. We generate 200 such synthetic data sets, and compute the Bayes factor between a TOP and 2G model for each of them. Extended Data Figure 4 shows the distribution of the log Bayes factor obtained from such a simulation. The red dashed line marks the log Bayes factor of 5.8 computed for the actual ANA data set. The false alarm probability of this Bayes factor is found to be 2.5%.

Now we get back to Extended Data Table 3 and provide some further interpretations into the results. First, we find that one can obtain a better fit of the neutron star mass function by adding a minimum- or maximum-mass cutoff or both to the 2G model. For example, the  $2G^{\max}$  model is favoured with a modest log Bayes factor of 1.1 against the 2G model for the ANA data set. This is in agreement with ref.<sup>16</sup>, where a log Bayes factor of 1.55 was found (albeit using a different set of neutron star mass measurements). In our analysis, again for the ANA data set, the model  $2G_{\min}^{\max}$  improves upon  $2G^{\max}$  with a log Bayes factor of 2.9. However, such a complex model with 7 free parameters is still disfavoured by a log Bayes factor of 1.8, in comparison to the TOP model. Therefore, we conclude that 1) the TOP model provides a simple and compelling fit to the neutron star mass function, no matter it is the observed masses or birth masses; 2) it is possible that future neutron star mass measurements will reveal more features in the mass spectrum, however we find no evidence of such features in current observations. The posterior median and  $1-\sigma$  credible intervals of TOP parameters, along with their prior ranges are given in Extended Data Table 4, to facilitate the usage of our model in future neutron star population studies.

In further comparison to previous studies, we note that the mass distribution of slow neutron stars in double neutron star systems was found to be uniform in ref.<sup>133</sup>, whereas the uniform model is disfavoured in our analysis for the SLOW dataset (see Extended Data Table 3). We first confirmed that we can reproduce the results of ref.<sup>133</sup> using the same data and comparing the same set of models. The discrepancy was largely due to a small number of measurements (12 versus 34). Additionally, the results of ref.<sup>133</sup> were also likely biased because of the incorrect assumption that the binary orbits of some double neutron star systems are randomly oriented<sup>3</sup>; a majority of binary pulsars in Extended Data Table 1 have measured inclination angles close to  $90^\circ$  (i.e., edge-on), which is the preferred orbital orientation for the pulsar mass to be measurable via Shapiro delays.

Extended Data Figure 5 shows the posterior distribution of model parameters of the TOP model for the OBS (in orange), ANA (in blue), and PHE (in black) data set. Comparing three cases, we find that although there are noticeable shifts, the three sets of posteriors are consistent with each other within uncertainties. This is because the accreted-mass corrections are comparable or smaller than the measurement uncertainties of original data. This plot also explains

---

<sup>3</sup>For this reason, we exclude in this work pulsar mass measurements that are dependent on the unknown binary orbital inclination angle.

why different accreted-mass prescriptions lead to similar model selection results in Extended Data Table 3.

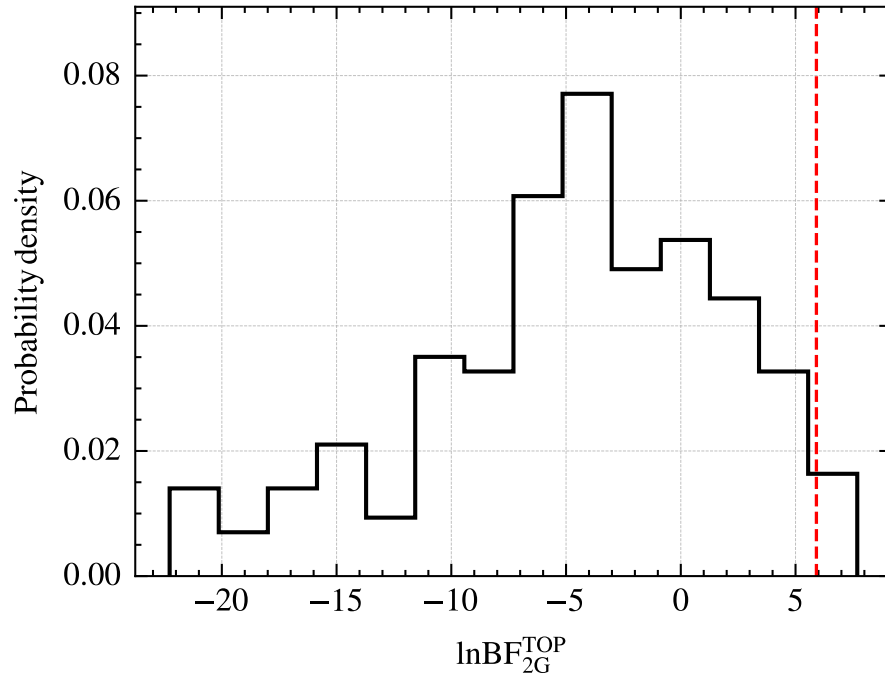
Extended Data Figure 6 shows the comparison of posterior distributions of the TOP model for different subsets of data. In the top panel, we demonstrate how the correction of accreted mass of recycled pulsars bridges the gap between two distinct subclasses – slow (SLOW) and recycled (REC) neutron stars. Although the uncertainties are large and therefore we cannot make conclusive statements, one can see that masses of recycled neutron stars are on average greater than those of slow neutron stars, and that our scheme accreted-mass corrections is effective because the  $\text{ANA}_{m_r}$  posterior distribution lies in between those of SLOW and REC. To test how our results are sensitive to the selection of neutron mass measurements obtained using different methods, we restrict our analyses to data from radio pulsar timing observations (denoted as  $\text{ANA}_{\text{radio}}$ ) and find that the TOP model is favoured against other models with similar significance (with respect to the full data set). In the bottom panel of Extended Data Figure 6, we show that the posterior distributions of the TOP model for the radio-only data set agree well with results of the full data set. The power-law index parameter  $\alpha$  is poorly measured for  $\text{ANA}_{\text{radio}}$  due to smaller number of measurements.

Extended Data Table 3: **The natural logarithm of Bayes factor between a listed model and a uniform distribution for different data sets.** Model names are: TOP – turn-on power law, G – Gaussian distribution, TOPG – turn-on power law plus a Gaussian peak, 2G and 3G indicates two- and three-component Gaussian distribution, respectively, SST – skewed Student’s t distribution, logN – log normal distribution, logU – log uniform distribution, Gamma – gamma distribution. The presence of a superscript or subscript indicates a maximum- or minimum-mass cutoff applied to the continuous distribution.

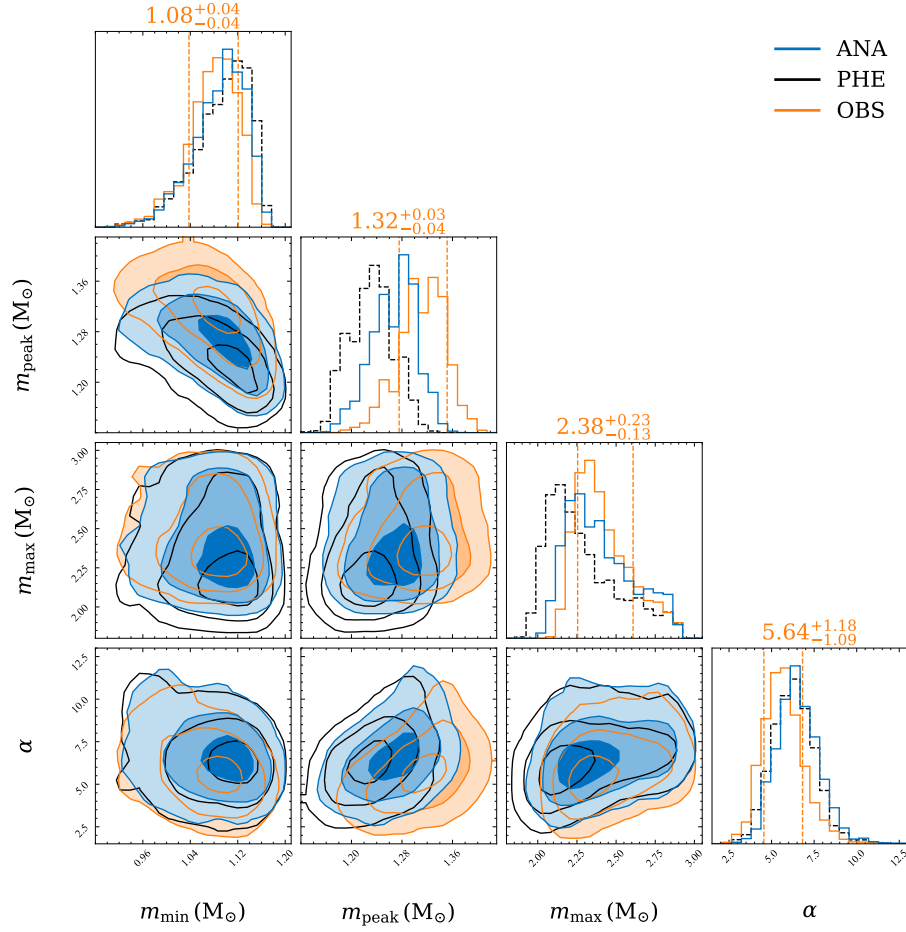
	OBS	ANA	PHE	ANA <sub>m<sub>r</sub></sub>	PHE <sub>m<sub>r</sub></sub>	REC	SLOW	ANA <sub>radio</sub>	OBS <sub>DNS</sub>
TOP <sup>max</sup>	13.2	16.1	13.1	8.7	6.3	6.2	4.4	22.1	5.3
TOP	12.2	15.4	12.2	8.5	5.4	5.1	4.5	22.0	5.2
TOPG <sup>max</sup>	11.1	14.4	12.4	7.0	5.1	4.0	2.4	19.5	3.5
2G <sub>min</sub> <sup>max</sup>	10.6	14.3	11.9	7.7	5.2	4.2	1.7	17.7	0.8
TOPG	9.3	12.3	9.2	4.9	2.6	2.5	2.0	19.3	3.4
G <sub>min</sub> <sup>max</sup>	8.5	9.9	7.5	4.2	2.8	2.5	1.2	15.2	1.6
2G <sub>min</sub>	8.5	12.4	9.4	5.7	3.1	2.4	0.6	16.4	−0.5
SST	8.3	11.4	8.5	5.1	2.5	2.6	1.3	17.1	0.1
G <sub>min</sub>	8.2	9.6	7.1	4.0	2.3	2.1	0.8	14.8	1.0
2G <sup>max</sup>	7.2	11.4	8.3	5.6	2.6	0.4	−0.2	16.3	−0.3
2G	6.8	10.3	6.6	4.2	1.1	−0.6	−1.3	15.1	−0.9
log U	5.5	6.0	5.1	3.5	3.1	3.2	1.4	4.8	0.5
3G	5.6	9.5	5.9	3.8	0.5	−1.0	−1.9	14.2	−2.3
log N	1.8	3.6	1.2	1.3	−0.6	−1.7	−1.0	12.8	2.2
Gamma	0.5	2.1	−0.4	0.6	−1.1	−2.4	−1.4	11.7	−1.8

Extended Data Table 4: **The priors, posteriors and 1- $\sigma$  credible intervals values for the TOP model using different data sets.**

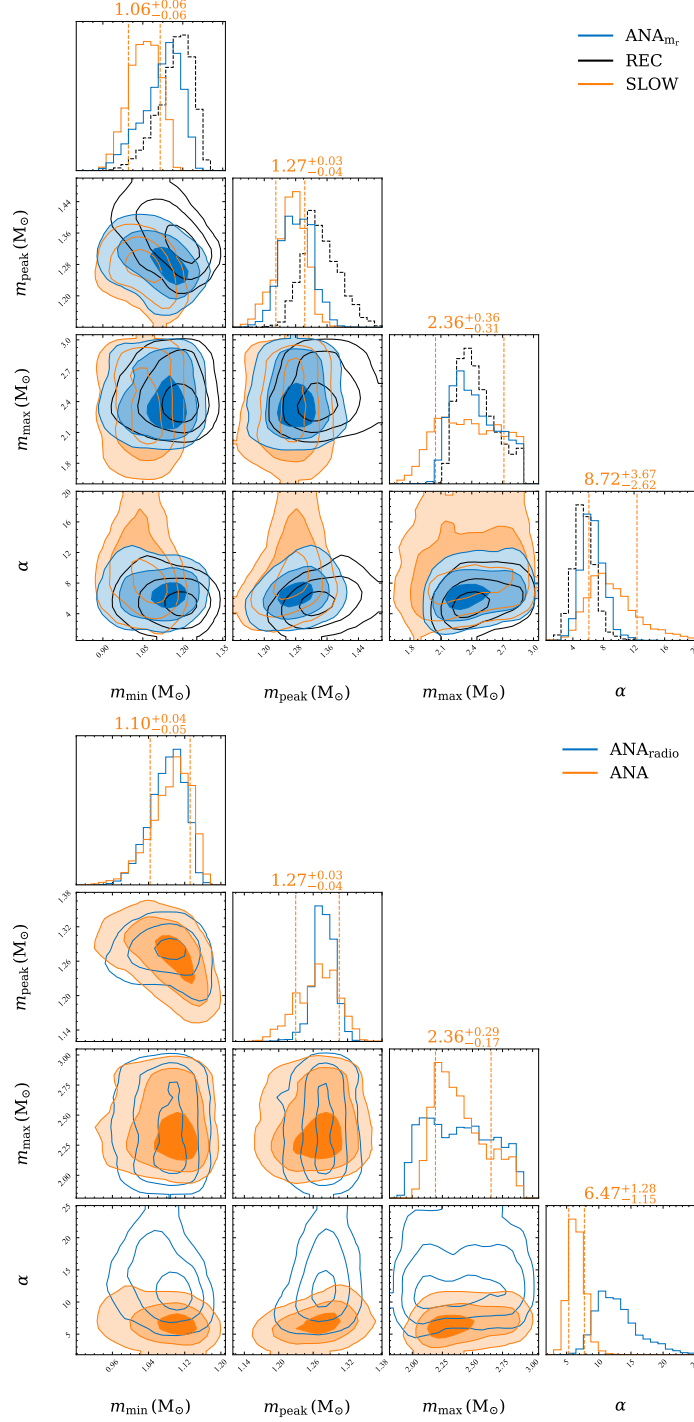
Model	Parameters	Prior	Posterior		
			OBS	ANA	PHE
TOP	$m_{\min} [M_{\odot}]$	$U[0.9, 1.5]$	$1.08^{+0.04}_{-0.04}$	$1.10^{+0.04}_{-0.05}$	$1.10^{+0.04}_{-0.06}$
	$\delta_m [M_{\odot}]$	$U[0.01, 1]$	$0.32^{+0.15}_{-0.12}$	$0.24^{+0.14}_{-0.11}$	$0.17^{+0.13}_{-0.10}$
	$m_{\max} [M_{\odot}]$	$U[1.5, 2.9]$	$2.38^{+0.23}_{-0.13}$	$2.36^{+0.29}_{-0.17}$	$2.23^{+0.33}_{-0.15}$
	$\alpha$	$U[-5, 25]$	$5.64^{+1.18}_{-1.09}$	$6.47^{+1.28}_{-1.15}$	$6.28^{+1.23}_{-1.19}$



**Extended Data Figure 4** The distribution of log Bayes factor (between the TOP and 2G model) for a simulated data set that includes 87 neutron star mass measurements drawn from a two-Gaussian distribution. The red dashed line is  $\ln\text{BF}_{2\text{G}}^{\text{TOP}} = 5.8$  computed for the actual ANA data set. This plot shows that the chance to falsely reject the two-Gaussian model for current observations of neutron stars is small, about 2.5%.



**Extended Data Figure 5** Posterior distribution of the TOP model parameters for the OBS (orange), ANA (blue) and PHE (black) data set. The vertical lines mark the 1- $\sigma$  credible interval of the marginalized posteriors for the OBS data set.



**Extended Data Figure 6** As Extended Data Figure 5, but for the ANA<sub>m<sub>r</sub></sub> (blue), SLOW (orange) and REC (black) data set on the top panel; and on the bottom panel for the ANA (orange) and ANA<sub>radio</sub> (blue) which is a subset of ANA by only including mass measurements from radio pulsar observations.

## F Semi-analytic supernova modeling

In this section we investigate the implications of the measured neutron star birth mass distribution for core-collapse supernova physics. Extended Data Figure 7a shows the distribution  $\phi(M_4)$  of the iron-silicon core mass  $M_4$  (defined by a threshold value of  $4 k_B$  per nucleon in specific entropy), weighted by the initial mass function (IMF) for massive stars,<sup>1,2</sup> for a set of 2912 single-star supernova progenitor models<sup>21</sup> with initial masses from  $9.45 M_\odot$  to  $45 M_\odot$ . The parameter  $M_4$  is a proxy for the mass coordinate for shock revival in neutrino-driven supernovae<sup>22</sup>. An additional factor  $(M_4/M_0)^{6.5}$  (with an arbitrary scaling factor  $M_0$ ) is applied to highlight deviations from the fiducial  $\phi(M_4) \propto M_4^{-6.5}$  scaling where the power-law slope comes from the TOP model as determined for the birth mass function (see Figure 4 in the main text).

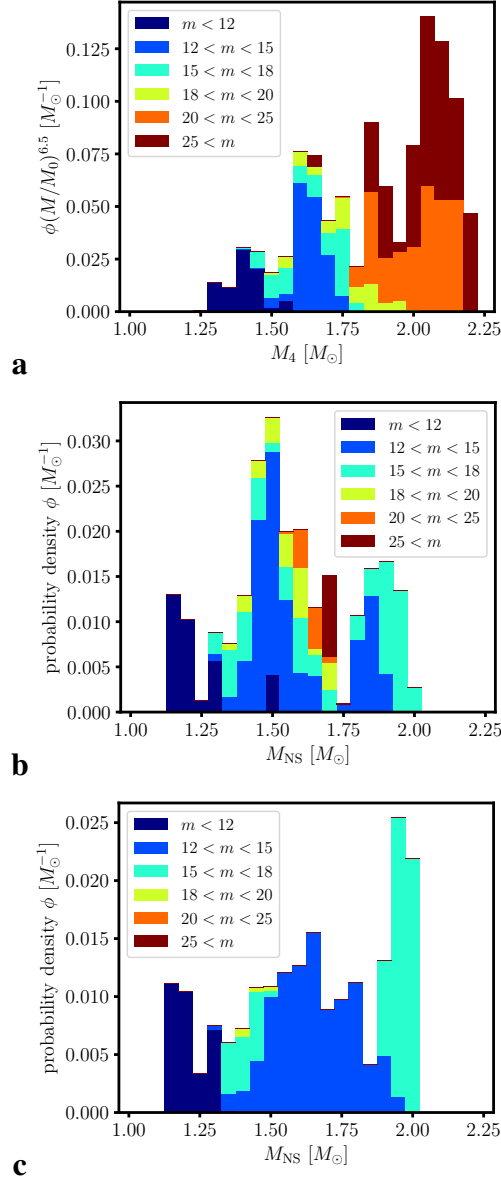
Without additional accretion after shock revival, the neutron star mass distribution would be expected to resemble the distribution of  $M_4$  because the neutron star mass is expected to scale linearly with  $M_4$ . Extended Data Figure 7a shows that this distribution not only shows multiple peaks, but is also top-heavy compared to the observed distribution of neutron star mass. The peaked nature of the theoretical neutron star mass distribution is found to persist in binary population synthesis simulations utilising modern semi-analytic supernova prescriptions<sup>139</sup>.

In order to flatten  $\phi(M_4)(M_4/M_0)^{6.5}$  (to make it look more like the distribution of observed neutron star masses), one either needs to remove neutron stars from the massive end of the distribution, or distribute neutron stars in the peaks more broadly towards higher masses. Applying the semi-analytic supernova model of Ref.<sup>21</sup> with default parameters, the resulting neutron star mass distribution deviates less from the  $M^{-6.5}$  power law because the model predicts most stars above  $20 M_\odot$  to collapse to black holes (Extended Data Figure 7b). The peaks from the distribution of  $M_4$  are still present, however, and a new peak around  $1.8 M_\odot$  emerges because shock revival does not occur at the edge of iron-silicon core, but at a mass shell further out.

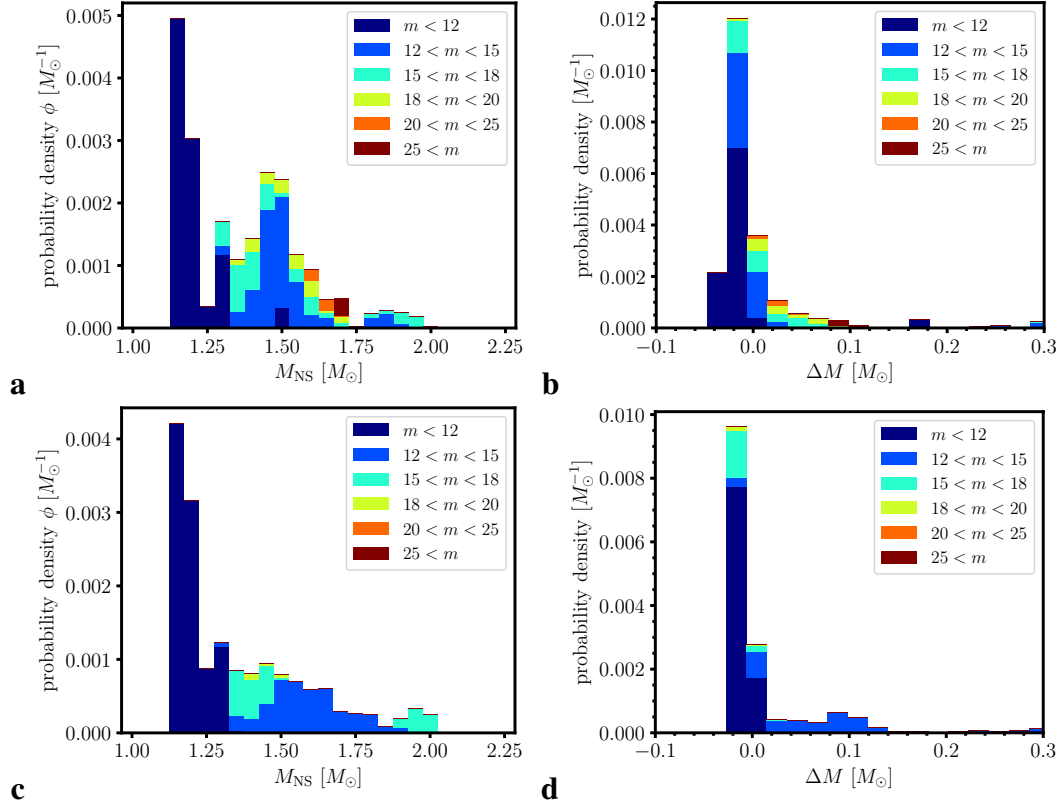
In order to improve the agreement between the semi-analytic supernova model and the observed distribution, we adjust the semi-analytic model to increase accretion after shock revival by reducing the shock compression ratio to  $\beta = 3.1$ , and to reduce the mass range for successful explosions while maintaining realistic explosion properties, as shown in Extended Data Figure 9. We choose a turbulent shock expansion multiplier  $\alpha_{\text{turb}} = 1.10$ , an efficiency  $\zeta = 0.85$  for the neutrino accretion luminosity and a cooling time scale  $\tau_{1.5} = 1.2$  s for a  $1.5 M_\odot$  neutron star. This broadens the peak at  $1.5 M_\odot$  in the standard model and shifts it to higher masses, bringing the mass distribution close to an  $M^{-6.5}$  power law up to  $M = 1.9 M_\odot$  (Extended Data Figure 7c and Extended Data Figure 8c).

The trough between low-mass neutron stars from stars with  $< 12 M_\odot$  is largely filled by a cluster of exploding progenitors around  $17 M_\odot$  (Extended Data Figure 9c). This is accom-

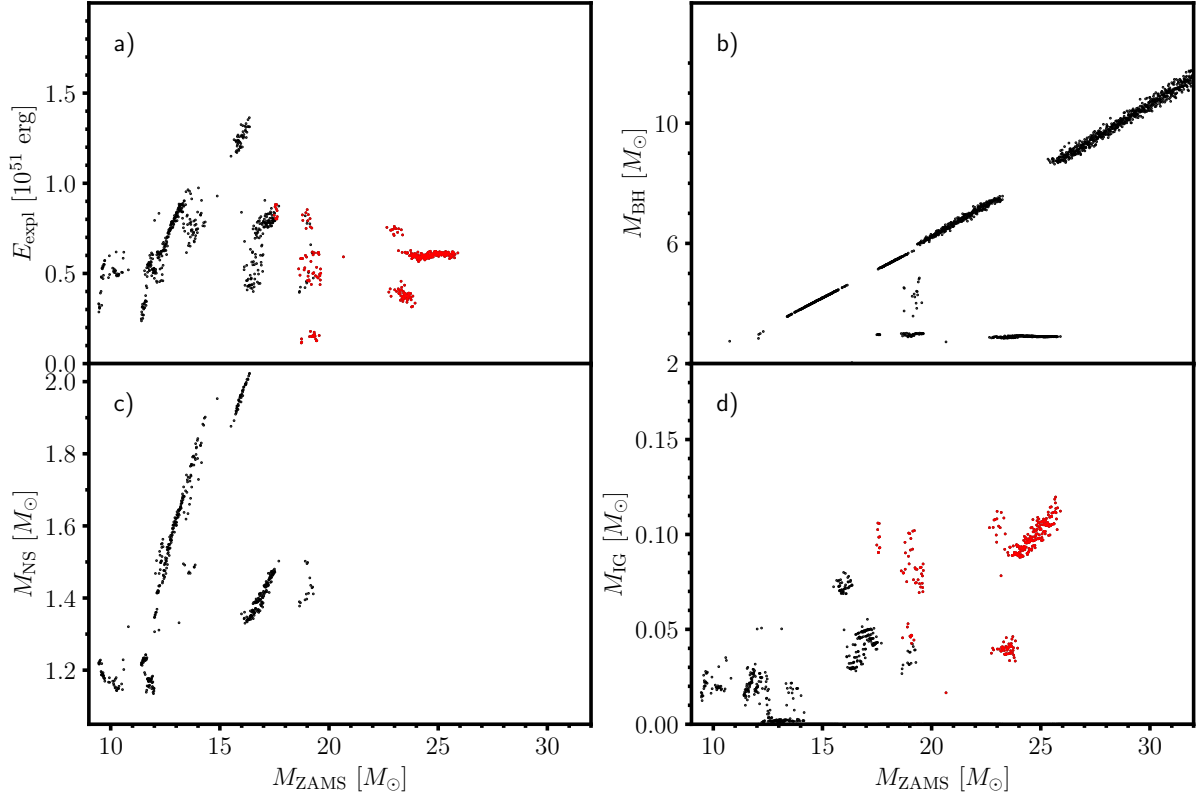
plished by allowing neutron stars from  $12\text{--}15M_{\odot}$  to accrete varying amounts of mass up to  $0.14 M_{\odot}$  after shock revival (Extended Data Figure 8). The predicted mass distribution still has (less prominent) troughs and a pile-up of neutron stars at  $2M_{\odot}$ , but these can be ascribed to imperfections in the semi-analytic supernova model. For light neutron stars, the model predicts unrealistically high net mass loss of up to  $0.04 M_{\odot}$  from the neutron star after early shock revival, which is not seen in multi-dimensional simulations. Under realistic conditions neutron stars from progenitors with  $< 12 M_{\odot}$  should therefore have higher masses and could fill the trough at  $1.25\text{--}1.4M_{\odot}$  in the distribution. The excess of very massive neutron stars around  $2 M_{\odot}$  could be removed in nature if roughly half of these neutron stars undergo more fallback to form black holes instead, or if many of the corresponding progenitors do not actually explode.



**Extended Data Figure 7** **a**, IMF-weighted distribution  $\phi(M_4)$  of the mass  $M_4$  of the iron-silicon core for a set of 2912 single-star supernova progenitors of solar metallicity<sup>21</sup>, with a compensation factor  $(M_4/M_0)^{6.5}$  to show deviations from the power-law of the measured neutron star mass distribution. **b**, Predicted distribution  $\phi(M)$  of neutron star masses with the same compensation factor based on the semi-analytic supernova model of ref.<sup>21</sup> with standard model parameters. **c**, Predicted distribution  $\phi(M)$  of neutron star masses with modified supernova model parameters to allow for more accretion after shock revival.



**Extended Data Figure 8** **a**, Predicted IMF-weighted neutron star mass distribution  $\phi(M)$  using the semi-analytic supernova model of ref.<sup>21</sup> with standard model parameters. **b**, Distribution of the amount  $\Delta M$  of net accretion after shock revival. Panels **c** and **d** Predicted IMF-weighted distribution of neutron star masses and accretion after shock revival for the modified supernova model with enhanced accretion during the explosion phase.



**Extended Data Figure 9** **a)** Explosion energy, **b)** black-hole masses for non-exploding cases and fallback supernovae, **c)** neutron star masses, **d)** nickel masses predicted by the semi-analytic supernova model with adjusted parameters for enhanced accretion to better match the observed power-law distribution of neutron star masses. Red dots in panels **a** and **d** denote explosions with black hole formation by fallback. Explosion energies and nickel masses span the typical range observed for Type IIP supernovae.

## G Potential selection effects

Here we discuss potential selection effects that might have had an impact on the inference of neutron star mass distribution. Our compilation of neutron-star mass measurements was the result of a diverse range of observations, which may have introduced different observation biases. For simplicity, we first focus on our main subset of data: masses measured with the radio pulsar timing method. Extended Data Figure 10a shows the measured mass versus the observed spin period for 39 recycled pulsars (blue) and other neutron stars (orange). Extended Data Figure 10b shows the measured mass versus the luminosity at 1.4 GHz calculated from the flux densities and pulsar distances as reported in the ATNF Pulsar Catalogue<sup>138</sup> for 39 recycled

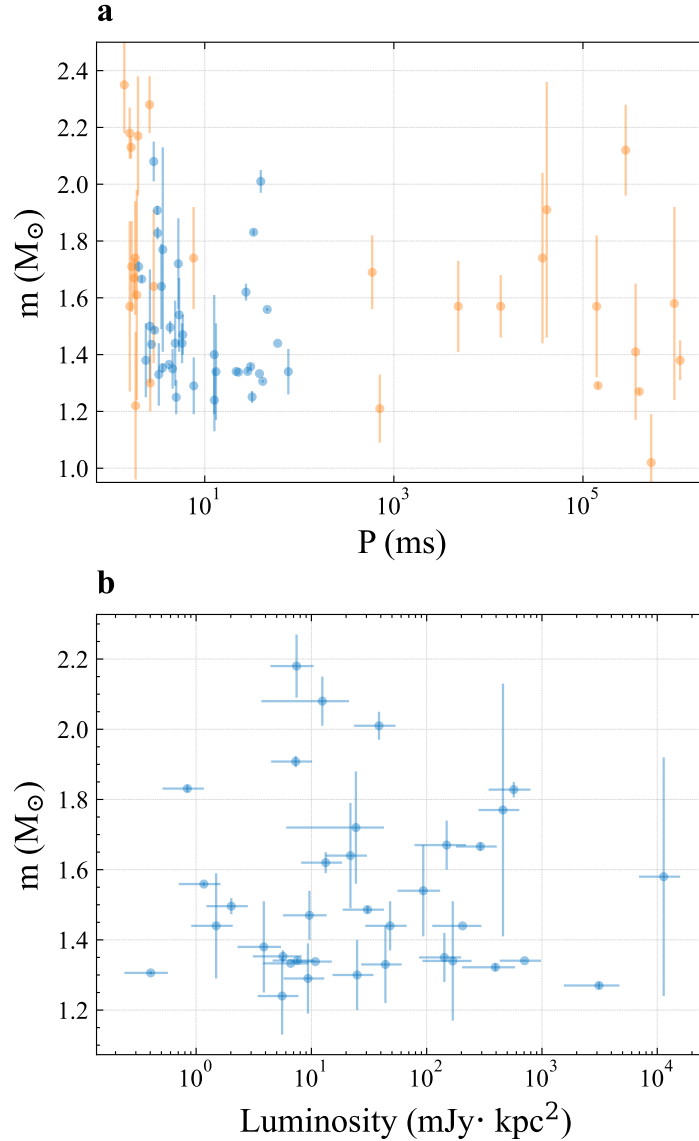
pulsars. From both plots, one can see that there is no apparent correlation between the mass and the detectability of a pulsar. This indicates that our inferred neutron-star mass distribution is unlikely to be biased by selection effects associated with pulsar surveys.

Another potential selection bias may have arisen because all but one of neutron stars in our compilation are in binary systems<sup>4</sup>. As massive stars, the progenitors of neutron stars, are commonly formed in binary systems, the neutron star mass function determined in this work may be a good representation of the overall neutron star population, except that binary systems containing neutron stars seen today are only a fraction of binary systems that have given birth to neutron stars. The supernova explosion associated with the formation of a neutron star could disrupt the binary system. If the survival probability of binary systems is correlated with the neutron star mass, for example, more massive neutron stars receive larger kicks at birth, then the population of observed binary pulsar systems would be biased towards a particular range of neutron star masses. The effect of such a correlation between the neutron star mass and the supernova kick has been tentatively investigated in population synthesis calculations<sup>139,140</sup>. In particular, using neutron star birth masses derived from modern, parameterized supernova models, ref.<sup>139</sup> found a neutron-star birth-mass distribution for the primary in double neutron star binaries that is skewed towards lower masses than the single-star mass function. Conversely, the mass distribution of secondaries is shifted upwards slightly compared to the single-star case (see their figure 7). Although the aggregated distribution of neutron star birth masses, in particular its shape, is like that of the single-star case, systematic differences in the slope of the mass distribution in double neutron stars, neutron star-white dwarf binaries and isolated neutron stars cannot be excluded; see, for example, figure 8a in ref.<sup>140</sup>. This will be an interesting area for future research with a much larger catalogue of neutron star mass measurements.

To summarize, although we believe that our results are robust against potential selection effects, we do expect to unveil a fuller picture of neutron-star mass function in the next decade or so when we have a sizeable sample of mass measurements for every subpopulation of neutron star systems, for example, binary neutron star mergers from gravitational-wave observations, neutron star and white dwarf binaries from pulsar observations, and isolated neutron stars from microlensing observations<sup>141,142</sup>.

---

<sup>4</sup>The one isolated neutron star (PSR J0030+0451) is a fully recycled pulsar. It was probably part of a disrupted binary system.



**Extended Data Figure 10 The period and luminosity distribution of pulsars with measured mass.** **a**, Measured mass versus spin period for 39 recycled pulsars (blue) in group *a* (“Modelling the accreted masses of recycled pulsars” in Methods) and the remaining neutron stars (orange). **b**, Measured mass versus luminosity at 1.4 GHz for 39 recycled pulsars, where the horizontal error bars account for uncertainties in the flux density and distance. We adopt the distance estimates from the Australia Telescope National Facility Pulsar Catalogue<sup>5</sup> while assuming a 20% error. In both panels, plotted are mean values with  $1\sigma$  credible errors, while the measurement uncertainty of spin periods in the upper panel is too small to be seen

<sup>5</sup><https://www.atnf.csiro.au/research/pulsar/psrcat/>

45. Tauris, T. M. *et al.* Formation of Double Neutron Star Systems. *Astrophys. J.* **846**, 170 (2017).
46. Chattopadhyay, D., Stevenson, S., Hurley, J. R., Bailes, M. & Broekgaarden, F. Modelling neutron star-black hole binaries: future pulsar surveys and gravitational wave detectors. *Mon. Not. R. Astron. Soc.* **504**, 3682–3710 (2021).
47. Broekgaarden, F. S. *et al.* Impact of Massive Binary Star and Cosmic Evolution on Gravitational Wave Observations I: Black Hole - Neutron Star Mergers. *Mon. Not. R. Astron. Soc.* **508**, 5028-5063 (2021).
48. Phinney, E. S. & Sigurdsson, S. Ejection of pulsars and binaries to the outskirts of globular clusters. *Nat.* **349**, 220–223 (1991).
49. Grindlay, J., Portegies Zwart, S. & McMillan, S. Short gamma-ray bursts from binary neutron star mergers in globular clusters. *Nature Physics* **2**, 116–119 (2006).
50. Lee, W. H., Ramirez-Ruiz, E. & van de Ven, G. Short Gamma-ray Bursts from Dynamically Assembled Compact Binaries in Globular Clusters: Pathways, Rates, Hydrodynamics, and Cosmological Setting. *Astrophys. J.* **720**, 953–975 (2010).
51. Ye, C. S. *et al.* On the Rate of Neutron Star Binary Mergers from Globular Clusters. *Astrophys. J. Lett.* **888**, L10 (2020).
52. Tauris, T. M. & Janka, H.-T. J0453+1559: A Neutron Star-White Dwarf Binary from a Thermonuclear Electron-capture Supernova? *Astrophys. J. Lett.* **886**, L20 (2019).
53. Abbott, B. P., Abbott, R., Abbott, T. D. & *et. al.* GW170817: Observation of Gravitational Waves from a Binary Neutron Star Inspiral. *Phys. Rev. Lett.* **119**, 161101 (2017).
54. Abbott, B. P., Abbott, R., Abbott, T. D. *et., al.* GW190425: Observation of a Compact Binary Coalescence with Total Mass  $\sim 3.4 M_{\odot}$ . *Astrophys. J. Lett.* **892**, L3 (2020).
55. Zhu, X.-J. & Ashton, G. Characterizing Astrophysical Binary Neutron Stars with Gravitational Waves. *Astrophys. J. Lett.* **902**, L12 (2020).
56. Abbott, R., Abbott, T. D., Abraham, S. & *et al.* Observation of Gravitational Waves from Two Neutron Star-Black Hole Coalescences. *Astrophys. J. Lett.* **915**, L5 (2021).
57. Abbott, R., Abbott, T. D., Acernese, F. & *et al.* GWTC-3: Compact Binary Coalescences Observed by LIGO and Virgo During the Second Part of the Third Observing Run. *Phys. Rev. X* **13**, 041039 (2023).
58. Ridolfi, A., Freire, P. C. C., Gupta, Y. & Ransom, S. M. Upgraded Giant Metrewave Radio Telescope timing of NGC 1851A: a possible millisecond pulsar - neutron star system. *Mon. Not. R. Astron. Soc.* **490**, 3860–3874 (2019).

59. Haniewicz, H. T. *et al.* Precise mass measurements for the double neutron star system J1829+2456. *Mon. Not. R. Astron. Soc.* **500**, 4620–4627 (2021).
60. van Leeuwen, J. *et al.* The Binary Companion of Young, Relativistic Pulsar J1906+0746. *Astrophys. J.* **798**, 118 (2015).
61. Fonseca, E., Stairs, I. H. & Thorsett, S. E. A Comprehensive Study of Relativistic Gravity Using PSR B1534+12. *Astrophys. J.* **787**, 82 (2014).
62. Kramer, M. *et al.* Tests of General Relativity from Timing the Double Pulsar. *Science* **314**, 97–102 (2006).
63. Lynch, R. S. *et al.* The Green Bank North Celestial Cap Pulsar Survey. III. 45 New Pulsar Timing Solutions. *Astrophys. J.* **859**, 93 (2018).
64. Cameron, A. D. *et al.* News and views regarding PSR J1757-1854, a highly-relativistic binary pulsar. In *Proc. 16th Marcel Grossmann Meeting (eds Ruffini, R. & Vereshchagin, G.)* 3774-3784 (World Scientific, 2022).
65. Ferdman, R. D. *et al.* PSR J1756-2251: a pulsar with a low-mass neutron star companion. *Mon. Not. R. Astron. Soc.* **443**, 2183–2196 (2014).
66. Jacoby, B. A. *et al.* Measurement of Orbital Decay in the Double Neutron Star Binary PSR B2127+11C. *Astrophys. J.* **644**, L113–L116 (2006).
67. Lynch, R. S., Freire, P. C. C., Ransom, S. M. & Jacoby, B. A. The Timing of Nine Globular Cluster Pulsars. *Astrophys. J.* **745**, 109 (2012).
68. Weisberg, J. M., Nice, D. J. & Taylor, J. H. Timing Measurements of the Relativistic Binary Pulsar PSR B1913+16. *Astrophys. J.* **722**, 1030–1034 (2010).
69. Martinez, J. G. *et al.* Pulsar J0453+1559: A Double Neutron Star System with a Large Mass Asymmetry. *Astrophys. J.* **812**, 143 (2015).
70. Ferdman, R. D. *et al.* Asymmetric mass ratios for bright double neutron-star mergers. *Nat.* **583**, 211–214 (2020).
71. Ferdman, R. D. *et al.* A Precise Mass Measurement of the Intermediate-Mass Binary Pulsar PSR J1802 - 2124. *Astrophys. J.* **711**, 764–771 (2010).
72. McKee, J. W. *et al.* A precise mass measurement of PSR J2045 + 3633. *Mon. Not. R. Astron. Soc.* **499**, 4082–4096 (2020).
73. Venkatraman Krishnan, V. *et al.* Lense-Thirring frame dragging induced by a fast-rotating white dwarf in a binary pulsar system. *Science* **367**, 577–580 (2020).

74. Arzoumanian, Z., Brazier, A., Burke-Spolaor, S. *et al.* The NANOGrav 11-year Data Set: High-precision Timing of 45 Millisecond Pulsars. *Astrophys. J. Supp.* **235**, 37 (2018).
75. Corongiu, A. *et al.* A Shapiro Delay Detection in the Binary System Hosting the Millisecond Pulsar PSR J1910-5959A. *Astrophys. J.* **760**, 100 (2012).
76. Zhu, W. W. *et al.* Mass Measurements for Two Binary Pulsars Discovered in the PALFA Survey. *Astrophys. J.* **881**, 165 (2019).
77. Stovall, K. *et al.* PSR J2234+0611: A New Laboratory for Stellar Evolution. *Astrophys. J.* **870**, 74 (2019).
78. van Kerkwijk, M. H. & Kulkarni, S. R. A Massive White Dwarf Companion to the Eccentric Binary Pulsar System PSR B2303+46. *Astrophys. J. Lett.* **516**, L25–L28 (1999).
79. Berezina, M. *et al.* The discovery of two mildly recycled binary pulsars in the Northern High Time Resolution Universe pulsar survey. *Mon. Not. R. Astron. Soc.* **470**, 4421–4433 (2017).
80. Archibald, A. M. *et al.* Universality of free fall from the orbital motion of a pulsar in a stellar triple system. *Nat.* **559**, 73–76 (2018).
81. Reardon, D. J. *et al.* Timing analysis for 20 millisecond pulsars in the Parkes Pulsar Timing Array. *Mon. Not. R. Astron. Soc.* **455**, 1751–1769 (2016).
82. Antoniadis, J. *et al.* The relativistic pulsar-white dwarf binary PSR J1738+0333 - I. Mass determination and evolutionary history. *Mon. Not. R. Astron. Soc.* **423**, 3316–3327 (2012).
83. Reardon, D. J. *et al.* The Parkes pulsar timing array second data release: timing analysis. *Mon. Not. R. Astron. Soc.* **507**, 2137–2153 (2021).
84. Desvignes, G. *et al.* High-precision timing of 42 millisecond pulsars with the European Pulsar Timing Array. *Mon. Not. R. Astron. Soc.* **458**, 3341–3380 (2016).
85. Serylak, M. *et al.* The eccentric millisecond pulsar, PSR J0955–6150. I. Pulse profile analysis, mass measurements, and constraints on binary evolution. *Astron. Astrophys.* **665**, A53 (2022).
86. Mata Sánchez, D., Istrate, A. G., van Kerkwijk, M. H., Breton, R. P. & Kaplan, D. L. PSR J1012+5307: a millisecond pulsar with an extremely low-mass white dwarf companion. *Mon. Not. R. Astron. Soc.* **494**, 4031–4042 (2020).
87. Barr, E. D. *et al.* A massive millisecond pulsar in an eccentric binary. *Mon. Not. R. Astron. Soc.* **465**, 1711–1719 (2017).

88. Guo, Y. J. *et al.* PSR J2222–0137. I. Improved physical parameters for the system. *Astron. Astrophys.* **654**, A16 (2021).
89. Fonseca, E., Cromartie, H. T., Pennucci, T. T. *et al.* Refined Mass and Geometric Measurements of the High-mass PSR J0740+6620. *Astrophys. J. Lett.* **915**, L12 (2021).
90. Yi, T. *et al.* A dynamically discovered and characterized non-accreting neutron star-M dwarf binary candidate. *Nature Astronomy* (2022).
91. Strader, J. *et al.* Optical Spectroscopy and Demographics of Redback Millisecond Pulsar Binaries. *Astrophys. J.* **872**, 42 (2019).
92. Clark, C. J. *et al.* Einstein@Home discovery of the gamma-ray millisecond pulsar PSR J2039-5617 confirms its predicted redback nature. *Mon. Not. R. Astron. Soc.* **502**, 915–934 (2021).
93. Deller, A. T. *et al.* A Parallax Distance and Mass Estimate for the Transitional Millisecond Pulsar System J1023+0038. *Astrophys. J. Lett.* **756**, L25 (2012).
94. Bellm, E. C. *et al.* Properties and Evolution of the Redback Millisecond Pulsar Binary PSR J2129-0429. *Astrophys. J.* **816**, 74 (2016).
95. Kandel, D. & Romani, R. W. Atmospheric Circulation on Black Widow Companions. *Astrophys. J.* **892**, 101 (2020).
96. Kennedy, M. R. *et al.* Measuring the mass of the black widow PSR J1555-2908. *Mon. Not. R. Astron. Soc.* **512**, 3001–3014 (2022).
97. Romani, R. W., Graham, M. L., Filippenko, A. V. & Zheng, W. PSR J1301+0833: A Kinematic Study of a Black-widow Pulsar. *Astrophys. J.* **833**, 138 (2016).
98. Romani, R. W., Kandel, D., Filippenko, A. V., Brink, T. G. & Zheng, W. PSR J1810+1744: Companion Darkening and a Precise High Neutron Star Mass. *Astrophys. J. Lett.* **908**, L46 (2021).
99. Nieder, L. *et al.* Discovery of a Gamma-Ray Black Widow Pulsar by GPU-accelerated Einstein@Home. *Astrophys. J. Lett.* **902**, L46 (2020).
100. Romani, R. W., Kandel, D., Filippenko, A. V., Brink, T. G. & Zheng, W. PSR J0952-0607: The Fastest and Heaviest Known Galactic Neutron Star. *Astrophys. J. Lett.* **934**, L17 (2022).
101. Miller, M. C. *et al.* PSR J0030+0451 Mass and Radius from NICER Data and Implications for the Properties of Neutron Star Matter. *Astrophys. J. Lett.* **887**, L24 (2019).

102. Riley, T. E. *et al.* A NICER View of PSR J0030+0451: Millisecond Pulsar Parameter Estimation. *Astrophys. J. Lett.* **887**, L21 (2019).
103. Özel, F. & Freire, P. Masses, Radii, and the Equation of State of Neutron Stars. *ARA&A* **54**, 401–440 (2016).
104. Iaria, R. *et al.* A possible cyclotron resonance scattering feature near 0.7 keV in X1822-371. *Astron. Astrophys.* **577**, A63 (2015).
105. Falanga, M. *et al.* Ephemeris, orbital decay, and masses of ten eclipsing high-mass X-ray binaries. *Astron. Astrophys.* **577**, A130 (2015).
106. Bhallerao, V. B., van Kerkwijk, M. H. & Harrison, F. A. Constraints on the Compact Object Mass in the Eclipsing High-mass X-Ray Binary XMMU J013236.7+303228 in M 33. *Astrophys. J.* **757**, 10 (2012).
107. Archibald, A. M. *et al.* A Radio Pulsar/X-ray Binary Link. *Science* **324**, 1411 (2009).
108. Wang, Z. *et al.* SDSS J102347.6+003841: A Millisecond Radio Pulsar Binary That Had a Hot Disk During 2000-2001. *Astrophys. J.* **703**, 2017–2023 (2009).
109. Ghosh, P. & Lamb, F. K. Diagnostics of disk-magnetosphere interaction in neutron star binaries. In van den Heuvel, E. P. J. & Rappaport, S. A. (eds.) *X-Ray Binaries and Recycled Pulsars*, vol. 377 of *NATO Advanced Study Institute (ASI) Series C*, 487–510 (1992).
110. Liu, X.-J., You, Z.-Q. & Zhu, X.-J. Observational evidence for a spin-up line in the P-Pdot diagram of millisecond pulsars. *Astrophys. J. Lett.* **934**, L2 (2022).
111. Archibald, R. F. *et al.* A High Braking Index for a Pulsar. *Astrophys. J. Lett.* **819**, L16 (2016).
112. Goldreich, P. & Reisenegger, A. Magnetic Field Decay in Isolated Neutron Stars. *Astrophys. J.* **395**, 250 (1992).
113. Bransgrove, A., Levin, Y. & Beloborodov, A. Magnetic field evolution of neutron stars - I. Basic formalism, numerical techniques and first results. *Mon. Not. R. Astron. Soc.* **473**, 2771–2790 (2018).
114. Spitkovsky, A. Time-dependent Force-free Pulsar Magnetospheres: Axisymmetric and Oblique Rotators. *Astrophys. J. Lett.* **648**, L51–L54 (2006).
115. Lattimer, J. M. & Schutz, B. F. Constraining the Equation of State with Moment of Inertia Measurements. *Astrophys. J.* **629**, 979–984 (2005).
116. Haensel, P., Zdunik, J. L., Bejger, M. & Lattimer, J. M. Keplerian frequency of uniformly rotating neutron stars and strange stars. *Astron. Astrophys.* **502**, 605–610 (2009).

117. Kalirai, J. S. The age of the Milky Way inner halo. *Nat.* **486**, 90–92 (2012).
118. Jofré, P. & Weiss, A. The age of the Milky Way halo stars from the Sloan Digital Sky Survey. *Astron. Astrophys.* **533**, A59 (2011).
119. Shklovskii, I. S. Possible Causes of the Secular Increase in Pulsar Periods. *Soviet Ast.* **13**, 562 (1970).
120. Damour, T. & Taylor, J. H. On the Orbital Period Change of the Binary Pulsar PSR 1913+16. *Astrophys. J.* **366**, 501 (1991).
121. Liu, X. J., Bassa, C. G. & Stappers, B. W. High-precision pulsar timing and spin frequency second derivatives. *Mon. Not. R. Astron. Soc.* **478**, 2359–2367 (2018).
122. Pathak, D. & Bagchi, M. Dynamical Effects in the Observed Rate of Change of the Orbital and the Spin Periods of Radio Pulsars: Improvement in the Method of Estimation and Its Implications. *Astrophys. J.* **868**, 123 (2018).
123. Lynch, R. S., Freire, P. C. C., Ransom, S. M. & Jacoby, B. A. The Timing of Nine Globular Cluster Pulsars. *Astrophys. J.* **745**, 109 (2012).
124. Freire, P. C. C. *et al.* Fermi Detection of a Luminous  $\gamma$ -Ray Pulsar in a Globular Cluster. *Science* **334**, 1107 (2011).
125. Abbott, B. P. *et al.* GW170817: Measurements of Neutron Star Radii and Equation of State. *Phys. Rev. Lett.* **121**, 161101 (2018).
126. Lattimer, J. M. & Prakash, M. Neutron Star Structure and the Equation of State. *Astrophys. J.* **550**, 426–442 (2001).
127. Kremer, K. *et al.* Formation of Low-mass Black Holes and Single Millisecond Pulsars in Globular Clusters. *Astrophys. J. Lett.* **934**, L1 (2022).
128. Tauris, T. M., Langer, N. & Kramer, M. Formation of millisecond pulsars with CO white dwarf companions - I. PSR J1614-2230: evidence for a neutron star born massive. *Mon. Not. R. Astron. Soc.* **416**, 2130–2142 (2011).
129. Lin, J. *et al.* LMXB and IMXB Evolution: I. The Binary Radio Pulsar PSR J1614-2230. *Astrophys. J.* **732**, 70 (2011).
130. Mandel, I., Farr, W. M. & Gair, J. R. Extracting distribution parameters from multiple uncertain observations with selection biases. *Mon. Not. R. Astron. Soc.* **486**, 1086–1093 (2019).

131. Thrane, E. & Talbot, C. An introduction to Bayesian inference in gravitational-wave astronomy: Parameter estimation, model selection, and hierarchical models. *Publ. Astron. Soc. Australia* **36**, e010 (2019).
132. Kass, R. E. & Raftery, A. E. Bayes factors. *Journal of the American Statistical Association* **90**, 773–795 (1995).
133. Farrow, N., Zhu, X.-J. & Thrane, E. The Mass Distribution of Galactic Double Neutron Stars. *Astrophys. J.* **876**, 18 (2019).
134. Ashton, G. *et al.* BILBY: A User-friendly Bayesian Inference Library for Gravitational-wave Astronomy. *Astrophys. J. Supp.* **241**, 27 (2019).
135. Talbot, C., Smith, R., Thrane, E. & Poole, G. B. Parallelized inference for gravitational-wave astronomy. *Phys. Rev. D* **100**, 043030 (2019).
136. Jones, M. C. & Faddy, M. A skew extension of the t-distribution, with applications. *Journal of the Royal Statistical Society: Series B (Statistical Methodology)* **65**, 159–174 (2003).
137. Wurtz, D., Chalabi, Y. & Luksan, L. Parameter estimation of arma models with garch/a-parch errors an r and splus software implementation. *Journal of Statistical Software* **55**, 28–33 (2006).
138. Manchester, R. N., Hobbs, G. B., Teoh, A. & Hobbs, M. The Australia Telescope National Facility Pulsar Catalogue. *Astron. J.* **129**, 1993–2006 (2005).
139. Vigna-Gómez, A. *et al.* On the formation history of Galactic double neutron stars. *Mon. Not. R. Astron. Soc.* **481**, 4009–4029 (2018).
140. Schneider, F. R. N., Podsiadlowski, P. & Müller, B. Pre-supernova evolution, compact-object masses, and explosion properties of stripped binary stars. *Astron. Astrophys.* **645**, A5 (2021).
141. Dai, S. *et al.* Gravitational Microlensing by Neutron Stars and Radio Pulsars: Event Rates, Timescale Distributions, and Mass Measurements. *Astrophys. J.* **802**, 120 (2015).
142. Wyrzykowski, Ł. & Mandel, I. Constraining the masses of microlensing black holes and the mass gap with Gaia DR2. *Astron. Astrophys.* **636**, A20 (2020).